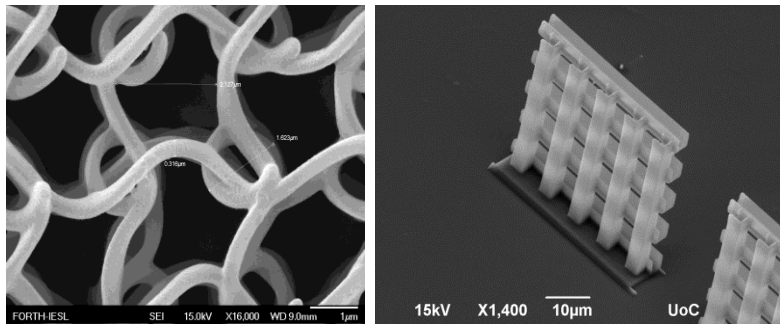


# UNIVERSITY OF CRETE

DEPARTMENT OF MATERIALS SCIENCE AND TECHNOLOGY

&

FOUNDATION FOR RESEARCH AND TECHNOLOGY HELLAS -  
INSTITUTE OF ELECTRONIC STRUCTURE AND LASER



## *3D Photonic structures fabricated by Direct Laser Writing*

Master Thesis of  
Aggelos Xomalis

Supervisors

Prof. Maria Kafesaki

Dr. Maria Farsari

HERAKLION, NOVEMBER 2015

~ 2 ~



## Abstract

The study illustrates the theory, fabrication and characterization of two photonic structures. The structures are fabricated in order to manipulate the light when passing through them and thus, exhibit a periodic well-defined structuring. We diverse our study in the fabrication of 3D silver Split Cube Resonators (SCR's) and gold/silver Helix structures.

### ***SCR's:***

A three-dimensional (3D) infra-red conductive metamaterial proposed for 90 degrees one way polarization rotator and asymmetric transmitter meta-device for linearly polarized light [1] is demonstrated. The metamaterial structure, which comprises of Split Cube Resonator (SCR) pairs rotated by 90 degrees with respect to each other along the wave propagation axis, was fabricated by direct laser writing and selective electroless silver coating, a straightforward, novel technique producing mechanically and chemically stable 3D photonic structures [10,11]. The asymmetric transmission (A.T.) response of the structure results from asymmetric interplay of electric and magnetic resonant responses of the SCRs, and equips the structure with almost total opaqueness along one propagation direction versus satisfying transparency along the opposite one, for linearly polarized incident way of a specific polarization. This asymmetric transmission response was also indirectly demonstrated experimentally through reflection measurements, in excellent agreement with the corresponding simulations. Additional simulations demonstrate that the 30% transmission asymmetry results from asymmetric polarization conversion, as is expected for reciprocal media, and it is associated with total opaqueness of the structure along the one propagation direction and with one-way 90° polarization rotation. These features, along with the possibility to modify the structure impedance adjusting properly the electric and magnetic responses of the SCRs make the structure an excellent candidate component for polarization conversion and isolation systems.

### ***Helix:***

Spiral structures that offer polarization control capabilities such as beam splitting effects, circular polarization creation and strong circular dichroism have been extensively studied by many research groups [16,21-22] in the last years. In order to fabricate a polarizer which leads to broadband response concerning the separation of Right handed Circular Polarization light (RCP) and the Left-handed one (LCP), we fabricate a spiral structure. The results indicate the blocking of LCP for more than 35 THz. The deviation of the two different polarizations are extremely high and recommends the structure for applications such as broadband circular polarizer, also we are able to create both gold and silver spiral structures with selective electroless plating, following a direct laser writing template formation.

The fabrication success for both structures was verified by the Scanning Electron Microscopy (SEM) and Electron Dispersion X-rays (EDX) characterization techniques. Moreover, we have the ability to characterize electromagnetically (FT-IR) the structures with both circular and linearly polarized waves.

## Table of Contents

<b>1 Theory of Electromagnetic Metamaterials .....</b>	
1.1 Definition of Metamaterials.....	7
1.2 History of electromagnetic materials and metamaterials .....	7
1.3 Split ring resonator: A novel metamaterial.....	8
1.4 Design of the proposed structures.....	10
1.4.1 Split Cube Resonators (SCR's) .....	10
1.4.2 Helical Structures.....	11
<b>2 Fabrication of Metamaterials .....</b>	
2.1 Fabrication process	
2.1.1 Theory of two-photon absorption.....	12
2.1.2 Mechanism of two-photon absorption .....	14
2.2 Direct Laser Writing	
2.2.1 Method.....	15
2.2.2 Substrate selection.....	19
2.2.3 Material synthesis.....	20
2.3 Metallization Process	
2.3.1 Gold metallization .....	23
2.3.2 Silver metallization.....	26
<b>3 Characterization of Metamaterials .....</b>	
3.1 Electromagnetic characterization of SCR system.....	29
3.1.1 Reflection measurements .....	29
3.1.2 Transmission properties: Asymmetric transmission.....	30
3.1.3 Polarization transformer response .....	32
3.2 Electromagnetic characterization of Helix .....	33
3.2.1 Scanning electron microscopy (SEM) characterization.....	33
3.2.2 Linear polarization characterization .....	34
3.2.3 Response to circularly polarized incident waves .....	36
<b>4 Conclusions-Future Aspects .....</b>	38
<b>References .....</b>	39
<b>Published work .....</b>	42
<b>Publication References .....</b>	56

# ***1. Theory of Electromagnetic Metamaterials***

## ***1.1 Definition of metamaterials***

*Electromagnetic metamaterials* are man-made structured materials which are used to manipulate electromagnetic waves. Their components can be dielectric or conductive materials; and their properties are not found usually in nature materials. The unique properties attainable by such metamaterials like negative index of refraction, rise from the well-defined structuring and their geometry. A diversion exists from other photonic structures such as photonic crystals: the operation wavelength in metamaterials should be greater than the unit cell size of the structure in order the structure to illustrate a homogenous material response. The building blocks of these metamaterials usually are called meta-atoms or meta-molecules.

## ***1.2 History of electromagnetic materials and metamaterials***

Investigation of materials for manipulating electromagnetic waves began at the end of the 19th century by *J. C. Bose*; in 1898 he studied substances with chiral properties. *K. F. Lindman* studied wave interaction with metallic helices as artificial chiral media early in 20th century. Moreover, *W. E. Kock* explicated materials that had similar properties to metamaterials, and artificial dielectrics were studied for antennas in the range of microwaves in the late 40s. Materials with negative index of refraction, named also left-handed metamaterials, were first proposed theoretically by *V. Veselago* at the end of 70's; he showed that such materials could transmit light showing also some unique propagation characteristics e.g. energy velocity opposite to the phase velocity [1-5]. The first who found a conventional way to create a left-handed metamaterial was *J. Pendry*, in 2000; Pendry's work was the one that led to a great exploration of the metamaterials research field.

### 1.3 Split ring resonator: A novel metamaterial

A *split-ring resonator (SRR)*, i.e. one or more concentric metallic rings with splits, is a man made structure which is involved in many research studies in the field of metamaterials. The reason for the huge utilization of this specific geometry is the achievement of the strong magnetic response with susceptibility even negative in number. The magnetic response of the SRR is a result of a magnetic resonance, where the SRR behaves as LC circuit [6,7,17]. The eigenfrequency  $\omega_{LC}$  of this LC resonator is

$$\omega_{LC} \sim (LC)^{-1/2},$$

with the inductance  $L$  produced by the loop current and the capacitance  $C$ , generated mainly in the split (Fig. 1) [14].

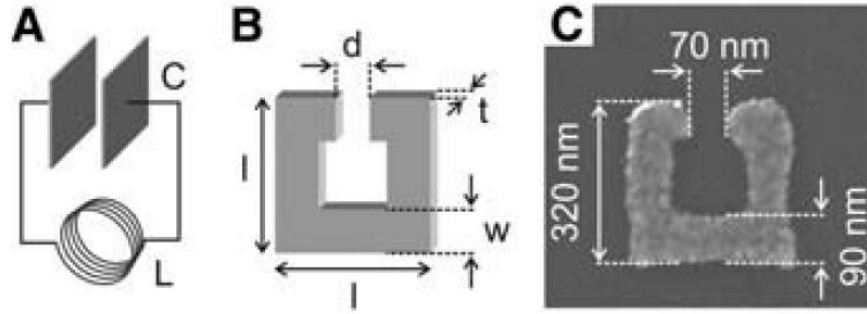


**Figure 1.** (A),(B) Demonstration of the analogy between LC circuit and Split Ring Resonator (SRR). (C) An electron beam lithography fabricated SRR [14].

A coupling to the LC resonance from a normally incident light is only possible if the vector of the electric field has a component parallel to the SRR capacitor (air gap); then the SRR which reacts as oscillator, acquires a resonant oscillating electric current, giving rise to a resonant local magnetic field [14]. If we close the capacitor/air-gap then we destroy the resonant magnetic response. This response is also not excited if the incident wave is polarized perpendicular to the SRR gap. This allows the coupling to the SRR magnetic resonance to be controlled through the polarization of the incident light. For such kind of structure (see Fig. 1B):

- The capacitance  $C$  and inductance  $L$  are given by:

$$C = \frac{\epsilon_o \epsilon_c w t}{d} \quad (1) \quad L = \frac{\mu_o l^2}{t} \quad (2)$$



- The eigenfrequency  $\omega_{LC}$  is:

$$\omega_{LC} = \frac{1}{\sqrt{LC}} = \left( \frac{c_0}{l\sqrt{\epsilon_c}} \right) \sqrt{\frac{d}{w}} \quad (3)$$

Thus, the corresponding wavelength  $\lambda_{LC}$  is:

$$\lambda_{LC} = l(2\pi)\sqrt{\epsilon_c} \sqrt{\frac{d}{w}} \quad (4)$$

In the above equations (Fig.1)  $d$  is the width of the gap of the capacitor,  $l$  is the size of the SRR,  $t$  is the metal thickness,  $w$  the width of the metal,  $\epsilon_0$  is the free space permittivity and  $\epsilon_c$  the relative permittivity. As we mentioned in the definition of metamaterials the wavelength  $\lambda_{LC}$  should be much bigger than the size of the unit cell. Thus, the incident wave can "see" a homogenous effective medium, i.e the structure (in our case a system of SRRs) illustrates a homogenous refractive index. This "effective" refractive index, along with the effective impedance of the structure, can be obtained through measurements or calculations of the reflection and transmission. Having the refractive index and impedance one can obtain the effective permeability ( $\mu$ ) and permittivity ( $\epsilon$ ) of the metamaterial under consideration.

To obtain a simple analytic formula of the magnetic permeability for a system of SRRs, one can use Kirchoff voltage rule, considering the SRR as a LC circuit excited by a perpendicular to the loop magnetic field (this corresponds to a plane wave propagating in the plane of SRR) [14, 27]. In that case we have  $U_C + U_L = U_{ext}$ , where the  $U_C$  is the voltage drop through the capacitance of the loop,  $U_L$  is the self-induction voltage of the inductance and  $U_{ext}$  the external magnetic flux. From Kirchoff's equation one can obtain the current in the SRR and from the current, which is  $m = IA$ , where  $I$  is the current of the loop and  $A = l^2$  its area.

- From the magnetic moment, one can obtain the magnetization,

$$M = \frac{N_C}{V} AI, \quad \frac{N_C}{V} = \frac{1}{a_{xy}^2 a_z} \quad (5)$$

where the  $N_C$  is the number of the SRRs in the system,  $V$  the volume of the structure,  $a_{xy}, a_z$  are the lattice constant in the plane and normal to the plane of the SRR [29, 30]. Then we use the magnetization as a function of magnetic susceptibility  $\chi_m$  and external field,  $H$ ,  $M = H\chi_m$ ,  $\mu(\omega) = 1 + \chi_m(\omega)$  and equation (2), and obtain the  $\mu$  as:

$$\mu(\omega) = 1 + \left( \frac{F\omega^2}{\omega_{LC}^2 - \omega^2} \right),$$

Where  $F = At/a_{xy}^2 a_z$  is a dimensionless quantity smaller than one (apart from  $\omega^2$  in the numerator, the rest of the fraction represents a Lorentz type resonance for a magnetic atom). If  $\omega$  is greater than  $\omega_{LC}$ , the magnetic permeability is negative,  $\mu(\omega) < 0$ ! Combining a system of SRRs, showing negative  $\mu$ , with a system of negative electrical permittivity, it can be shown that the resulting index of refraction  $n = \sqrt{\epsilon\mu}$  becomes negative, thus the structure characterized as negative index metamaterial.

The most common negative electrical permittivity material is a system of thin metallic wires. In accordance with literature [9] which shows that the combined SRR and wire systems lead to both magnetic and electric response, we decided to combine both responses in a single element, a split cube resonator (see Fig. 4), which has the possibility of free standing with fully volumetric geometry, and allows a much larger variety of structure designs and high transmission values due to the substrate of supporter [10].

#### 1.4 Design of the proposed structures

##### 1.4.1 SCR's:

Figure 4 presents the unit cell of our first three dimensional conductive metamaterial which is studied in the present thesis, it consists of two *Split-Cube Resonator* structures rotated by  $90^\circ$  with respect to each other along the propagation direction (z axis). Interestingly, the structure lacks mirror symmetry along all the three axis (x, y and z) as well as  $C_4$  rotational symmetry in the x-y plane. According to the literature, [16,17] structures of this rotational symmetry are expected to allow asymmetric transmission for linearly polarized waves. This comes from asymmetric cross-polarization conversion of a linearly polarized wave incident on the two opposite sides of the slab along the propagation direction and depends strongly on the polarization of the incident wave in the x-y plane.

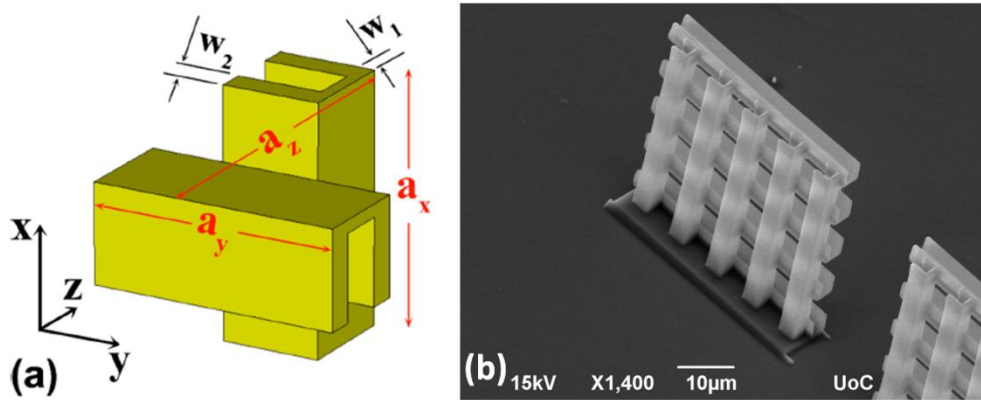


**Figure 4.** (a) The building block of the three dimensional SCR metamaterial. The dimensions of the fabricated structure are  $a_x = a_y = 8.0 \mu\text{m}$ ,  $a_z = 9.1 \mu\text{m}$ ,  $w_1 = 600 \text{ nm}$ , and  $w_2 = 850 \text{ nm}$ , respectively. The wave propagation is along the z-direction. (b) Top view of the SEM image of the 3D SCR metamaterials under consideration, recorded at x1400 zoom. The magnification scale can be seen below the SEM image, the structure dimensions are  $40 \times 40 \mu\text{m}$ .

### 1.4.2 Helix:

Another interesting system that we studied here is that of an helix-type resonator. This can be considered also derived from the SRR by pulling the one edge out of the 2D plane [20,21]. This kind of helix/spiral geometry is similar to a 90 degrees twisted SRR dimer system [22]. The interplay of electric and magnetic interactions in SRR dimmers leads to unique optical properties that can be controlled by twisting the one dimmer with respect to the other.

Figure 5 shows our helix geometry (two pitches), where we investigate the transmission for both Left handed Circularly (LCP/ $T_{++}$ ) and the Right handed Circular (RCP/ $T_{--}$ ) polarized light. The results demonstrate strong and broadband extinction of one of the two different polarizations which, recommends the structure for applications such as broadband circular polarizer. Using selective electroless plating we were able to create both gold and silver structures. The geometrical structure parameters for the structure as fabricated and characterized experimentally are detailed in Figure 5.

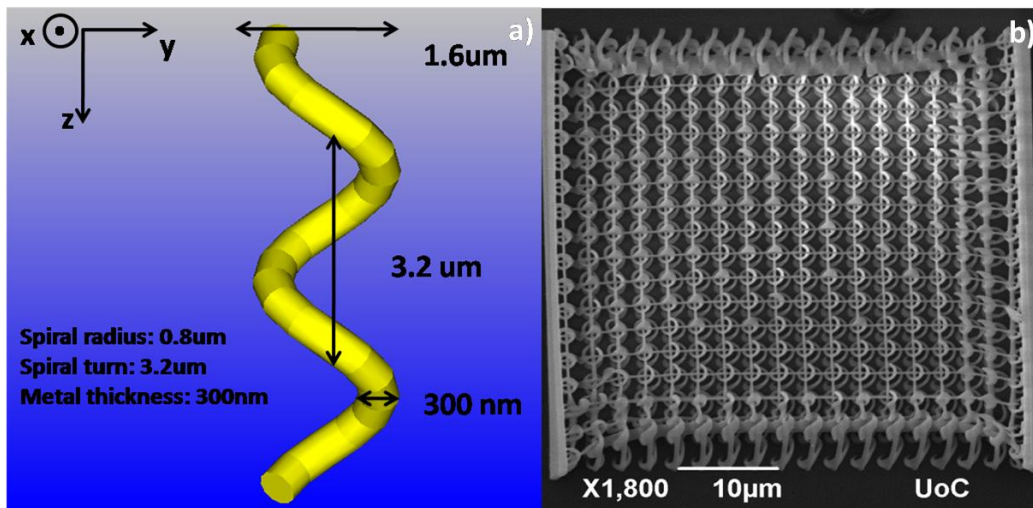


**Figure 5.**(a) The unit cell of the 3D freestanding spiral polarizer; the electromagnetic wave propagates along the z-direction. (b) Top view of the SEM image of the 3D photonic metamaterial made by helical particles as the one of panel (a); the size of the structure is 35 μm.

## 2. *Fabrication of Metamaterials*

As we mentioned earlier the structures analyzed in this work have been fabricated by *direct laser writing (DLW)*, followed by *electroless* gold and silver *plating*. Direct laser writing usually utilizes femtosecond laser pulses to impel two photon absorption (non-linear phenomenon) of a photosensitive molecule (in our case photoinitiator) into the volume of a monomeric mixture, this molecule after the irradiation creates free radicals and starts the polymerization procedure. Thus, in the next chapter we introduce the theory of the two photon absorption, the mechanism of the two photon polymerization and the fabrication technique.

### 2.1 *Theory of two-photon absorption*

#### 2.1.1 *Two photon absorption*

Two photon absorption (TPA) is the procedure which describes the excitation of molecule or atom from a lower energy state e.g.  $|n\rangle$  (which can be the ground state) to next higher energy level  $|n + 1\rangle$ ; after the absorption of two photons (non-linear phenomenon). In TPA transition, an atom/molecule is taken to an excited state by simultaneously absorbing two photons in a single quantum event. It is known that the probability of n-photon absorption is proportional to the  $n^{\text{th}}$  power of the photon flow density. Thus, high population density of photons is required in order to observe this phenomenon. Furthermore, high density of photons urgently required in time and space. Thus, this kind of non linear phenomenon takes place only at focal point of laser beam. Usually, these high flow densities can easily provided by a femtosecond laser source.

The theory of TPA was theoretically predicted by Maria Coppert-Mayer in 1931(during her PhD studies) and was experimentally observed for the first time in 1961 when the invention of lasers took place. Moreover, Isaac Abella experimentally proves the effect of TPA by using Cesium vapor as the two-photon absorbing material, in 1962. TPA is a multiple photon excitation

approach that can initiate photochemical changes, like e.g. photopolymerization. Most of the photoresistances which polymerize under ultraviolet irradiation ( $hf$ ) exposure can incur similar reactions when two photons ( $hf/2$ ) are absorbed, provided that the light intensity is high enough. Two mechanisms have been reported for TPA Figure 6.

The first mechanism indicates on the existence of a real interstitial state, from which an already excited electron is further pumped to a higher energy level by absorbing a single photon. Then can absorb a second photon in order to pump to  $S_2$  energy state (Fig. 6a). Such a process is termed stepwise TPA. Compared to simultaneous TPA (Fig. 6b), stepwise TPA does not require coherence of the laser source, and can be considered as two separate consequential single photon absorption reactions.

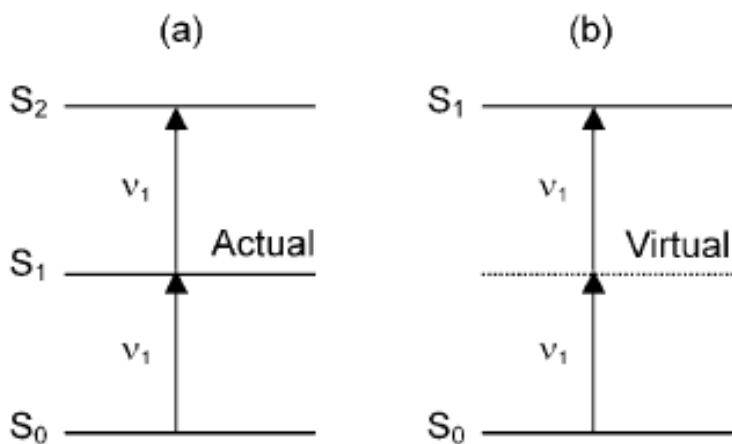


**Figure 6.** Mechanisms of TPA: (a) stepwise excitation, (b) simultaneous two photon excitation.

Concerning the simultaneous TPA, virtual intermediate states exist. These states are created by the interaction of the absorbing species with the first photon. Whether, a second photon with the same energy arrives in the virtual state lifetime of the first one; then the energies of the two photons added together and the molecule or the atom pumped to the excited state. Thus, it is apparent that higher intensities are required for the simultaneous TPA, which usually requires femtosecond pulsed lasers with enough high repetition rate of pulses. For femtosecond laser micro-fabrication, simultaneous TPA is more accurate.

The photons that partake in the transition are able to have a time interval given by the formula:  $\hbar/\Delta S$  (principle of Heisenberg), where  $\Delta S$  is the difference of energy between the molecule's virtual state and the next real state, and  $\hbar$  is the Planck constant. Consequently, the absorption of two photons does not need to be totally instantaneous, once it occurs in an intermission given by the Heisenberg principle.

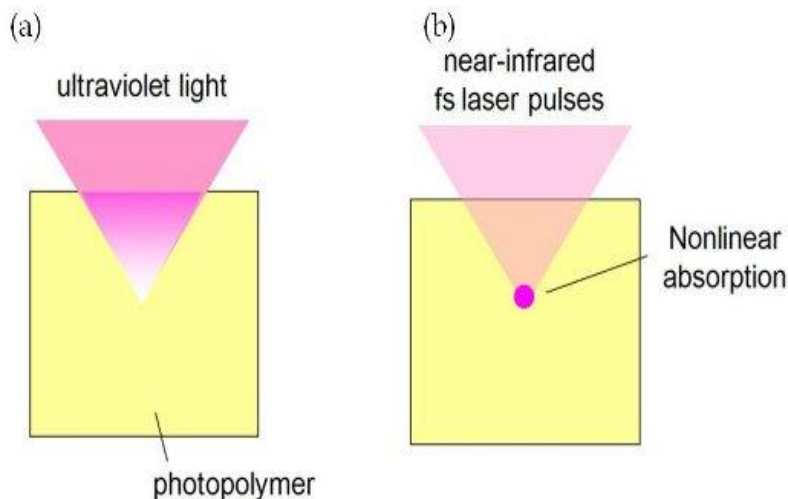


**Figure 7.** The laser beam in single-photon polymerization (a), and in two photon polymerization (b) (By Hiroaki Nishiyama and Yoshinori Hirata, Osaka University, Japan). The darker magenta color shows the polymerized material.

### ***2.1.2 Mechanism of two photon polymerization***

Photo-polymerization is the reaction of the light with photosensitive materials, after the exposure of this kind of materials to light with specific wavelength solidification takes place. More specifically, when a laser beam of high intensity is focused into the volume of a liquid or gel photosensitive material that is transparent to near-infrared (NIR) light, the photoinitiator that is used to enhance two photon activation, is excited by the simultaneous absorption of two photons, and results in the generation of free radicals (initiation). This is the beginning of a free radical polymerization. The radicals formed react with monomers, producing monomer radicals which participate in a chain reaction (propagation). This reaction will continue until the monomers are consumed, or until two growing radicals meet (termination).

This procedure is described the reactions (a)-(d) shown in Fig. 8. A point of attention is the solubility of the photosensitive molecules, which usually are in powder form, to the mixture of monomers. If the photosensitive molecules- photoinitiators are soluble in the hydrophobic mixture, then provides desirable free radicals after the irradiation; and thus the monomeric material can polymerized. We have the advantage in our lab to synthesize the photosensitive materials, and moreover to test multiple photoinitiators. It is important to control the volume of the materials which polymerized every time, in order to obtain polymeric structures with high resolution. In view of the above mentioned consideration, we placed in the mix of the material a molecule which acts as radical quencher. By that, we achieved control with great spatial resolution the polymerization volume. Briefly, polymerization by light irradiation defined as the chemical reaction that transforms the independent/repeating units (monomers) to macromolecule chains (polymers).

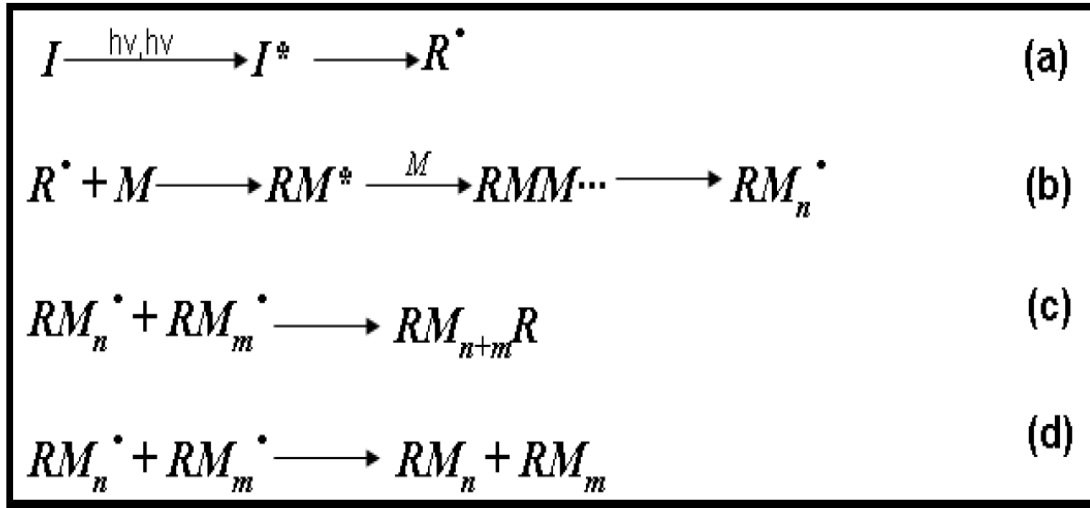


**Figure 8.** Polymerization process. Loose Matter Laboratory. Department of Material Science and Technology. University of Crete.

## 2.2 Direct Laser Writing

### 2.2.1 Method

The growing and imperative demand of nanotechnology for increasingly smaller devices has incited the invention of several methods and techniques owing the potential to manufacture structures and devices beyond anything ordinary so far [11,12]. These techniques have already been adopted by research laboratories worldwide and are in use throughout industry oriented towards the matter micro-manipulation.

Direct Laser Writing (DLW), is a technique in which directly a surface or material exposed to laser irradiation. In others words, that technique is likened with pen which can write precisely and selectively to substrates. Many different research field use DLW for applications e.g. the electronic properties of graphene-based devices can controlled by simple writing circuits on it[13]. Also, flexible graphene emitters fabricated by DLW are already proposed [14-16]. The majority of the groups worldwide uses DLW for the fabrication of dielectric polymeric scaffolds, in order to obtain photonic crystals and scaffolds for tissue engineering or for bone restoration application [17-20].

As far as it concerns our fabrication approach, the DLW method, it is a 3D printing technology allowing the fabrication of 3D structures with resolution below 100 nm. Briefly, the beam of an ultrafast laser is tightly focused inside the volume of a transparent and photosensitive material, causing it to absorb two or more photons and polymerize locally. By moving the beam in three dimensions inside the photopolymer volume, one can fabricate 3D structures of great accuracy.

DLW is based on the principles of stereolithography with the difference that DLW relies on two photon absorption (TPA) to initiate the polymerization of the hybrid photo-structurable material. The majority of the photosensitive materials are usually transparent at the infrared (IR) light and highly absorbing at the ultraviolet (UV) spectral region. An ultrafast laser emitting at 800 nm with pulse duration less than 20 femtoseconds induces the absorption of two IR photons of energy  $hf/2$  each by the material instead of the absorption of a single photon of energy  $hf$ .

The absorption of two photons takes place only under high intensity conditions; that is to say at the focal spot of the laser beam where these conditions are fulfilled. The TPA rate is proportional to the square of the laser intensity. This quadratic dependence of TPA on laser intensity enables the confinement of the photochemical changes into submicron dimensions near the focal point, where the laser intensity exceeds a certain threshold value for TPA. The photochemical reactions can be initiated at the volume below the diffraction-limit by controlling the laser energy and the number of the applied pulses because of the threshold behavior of TPA.

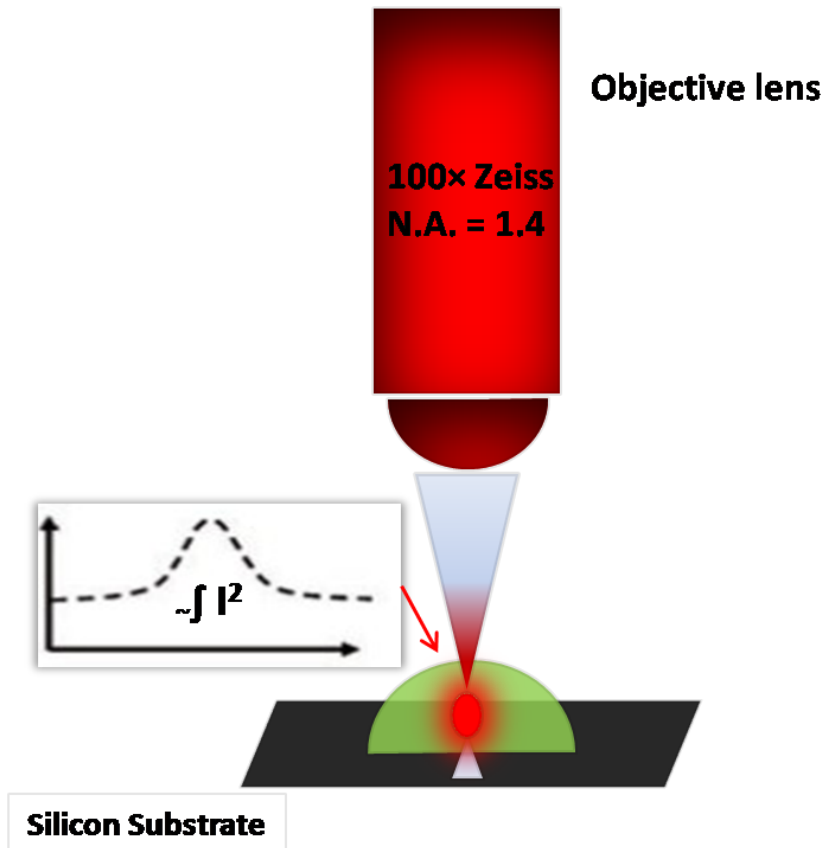


**Figure 9.** The *DLW* process: The laser beam is collected by a lens (100x N.A.=1.4) and focused into the volume of the hybrid organic-inorganic photosensitive material. The polymerization will take place only at the focal spot of the laser beam. The structure is fabricated on a silicon substrate in order to be used for straightforward transmission measurements.



DLW is an outstanding technique for micro-fabrication with great spatial resolution, offering the potential for exceptional structures fabrication, beyond the diffraction limit. A large variety of structure designs were constructed in our lab, some of those demonstrated in the figure below. Figure 10 a) demonstrates a micro drum which was fabricated on the edge of the optical fiber; this project brings the DLW achievements to optical fiber environment. Moreover Figure 10 b,c) corresponds to tissue engineering application; Figure 10 b) shows a Burr-like, laser-made 3D micro scaffolds for tissue spheroid encasement. Figure 10 c) demonstrates structure which used for cell scaffold; and specifically for bone cells cultivation [17-19]. Figure 10 d) proves that the DLW technique can obtain structures of any size and morphology. Recently, our group started to work on a new project concerning the fabrication of three dimensional structures with total size more than 1mm x 1mm; until now the fabrication of such big structures was impossible. Only two dimensional photolithography techniques, such as stereolithography, allow the UV irradiation of such large surfaces. Thus, 2D patterns of polymerized material are possible to fabricate.

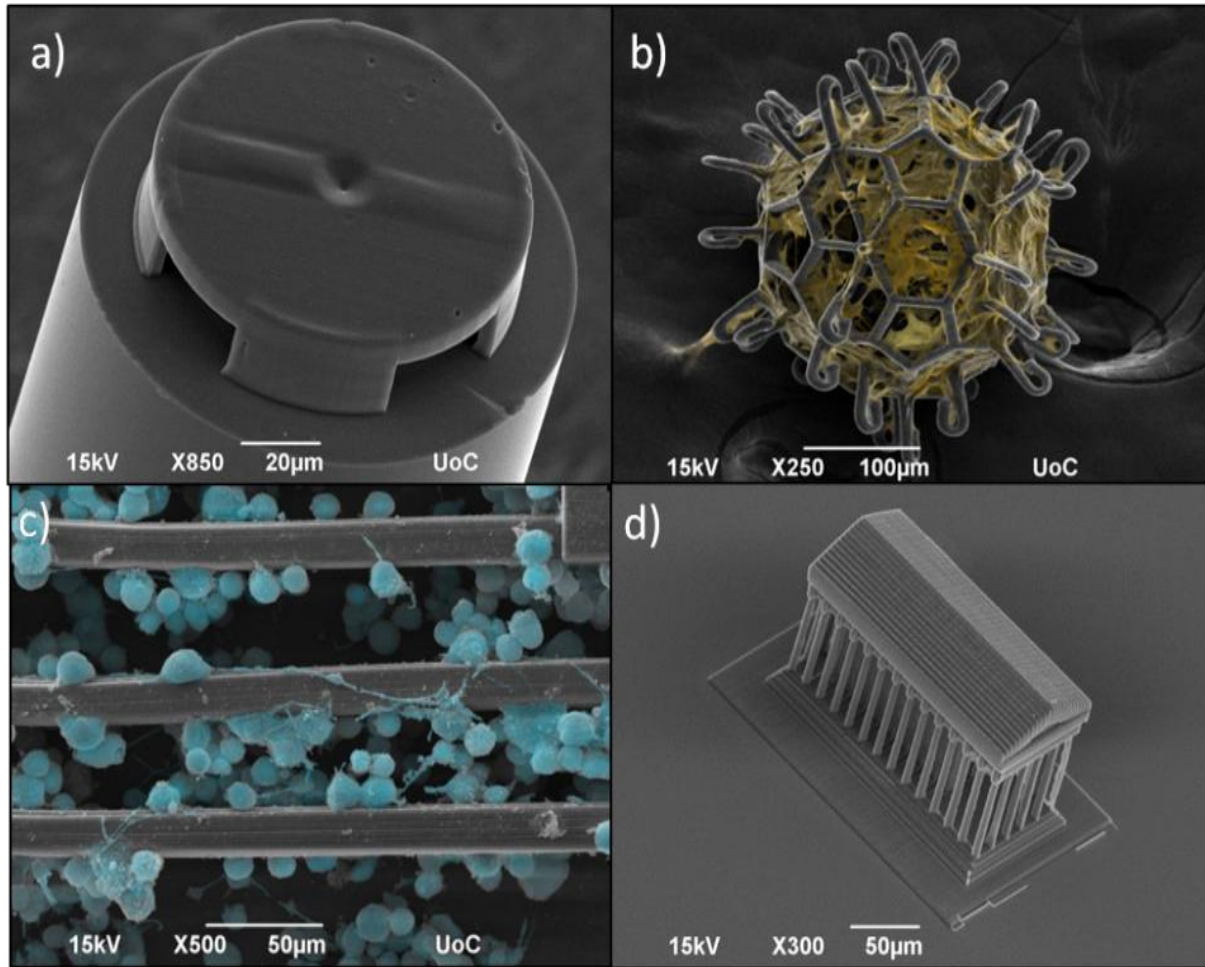


**Figure 10.** (a) A micro drum DLW-fabricated at the tip of an optical fiber: such kind of structures is very promising for sensing gases or liquids (b),(c) False colored cells cultures on DLW-fabricated 3D for tissue engineering applications. (d) The potential of our technique is able to face all the difficulties of a structure design.

In our case the set up it consist of a Ti-Sapphire femtosecond pulse laser, operated at 800nm wavelength with repetition rate 75MHz and duration of pulses less than 20 fs. Through a dichroic mirror and a CCD camera we are able to watch live the printing/writing process, which gives the advantage to fabricate structures with great accuracy and control. The sample placed on piezoelectric stages which can move in three axis, thus the three dimensional printing can be possible. The structure fabricated layer by layer with the last layer on the surface of the photosensitive material and the substrate. Moreover, with an acousto-optic modulator-shutter which allows the intensity of light to be controlled and modulated even up to 50 MHz; we can block and unblock the laser beam fast enough. Finally, we use an attenuator to change precisely the intensity of the laser beam which irradiates the sample, thus to the same sample we can have structures created by different laser intensities.

Alignment of the laser beam is necessary before the fabrication process. The laser beam passes from many mirrors, beam splitters and attenuators before reach the sample, and thus a simple misalignment of the laser beam can lead to wrong focus point. So, if we manage to bring the beam in the correct position before the objective lens then the fabrication procedure leads to good structures without any interruption of the shape and the size.

We can use DLW in many research fields, and thus this makes the technique unique. Our lab divided to two major research fields. First is the photonic and metamaterials field which concerns the fabrication and metallization of photonic crystals and metamaterials. Another field is the fabrication of polymeric scaffolds which can use for cell cultivation. Subsequently, the structures/scaffolds are suitable to use for tissue engineering e.g. tissue repairing and bone restoration. Moreover, we explore fabrication of structures in the environment of the optical fiber (see Fig.a) aiming to micro sensor devises with extraordinary sensitivity at minimum volumes of gases. The great spatial resolution that DLW offers is suitable for the fabrication of complex three dimensional structures beyond the diffraction limit. The material which used as template is a liquid/gel mix of organic, inorganic components with photosensitive molecules, and we will analyze it to the next paragraphs. The exposure of the material to UV light leads to solidification, thus different properties exhibit to the irradiated material e.g. different viscosity, refractive index, mechanical modulus etc.

The polymerized material present different refractive index from the monomeric one, thus the beam should pass only once from the volume of the photosensitive material, in order to avoid any further refraction of the focused beam. We should say to this point that the drop of the photosensitivity material placed to substrate. All the previous consideration concerns a transparent substrate at the infrared region; in order to obtain application at THz region. These kind of substrates usually are Silicon Oxide close to ~100um thick, unfortunately these cover slips are opaque to few THz frequencies, and thus we should explore the fabrication of the structures to other substrates. A critical characteristic of the substrate is that should not interact in any way with photo-structurable material.

### 2.2.2 Substrate selection

Until now all the experimental measurements concern only reflection because of the opacity of the substrate. For the first time we can use other materials for substrate which are more transparent in the range of frequencies that we work (e.g. silicon  $\text{Trans} > 55\%$ ). To make this happen we should fabricate our structure in a different way, now the focused laser beam can't be passing through substrate because silicon isn't transparent in the optical-infrared wavelengths. So we place the sample upside down with material face the objective lens. We must be very careful because this time we close the sample from the side of the material.

Also we use an objective lens with high numerical aperture ( $100\times$ , N.A. = 1.4, Zeiss, Plan Apochromat) in order to achieve the minimum polymerization volume. Therefore immersion oil (with the same refractive index as the glass) added between the lens and the material surface which allows the beam without any refraction reach in the volume of the material. Point of attention is that we should avoid leaving the material in contact with the immersion oil for longer time than the writing process because the material drifts away from the oil. Thus, after the end of the fabrication procedure we remove and clean carefully with a mix of ethanol and double distilled water (ratio 8:2) first the objective lens and then the oil from the sample.

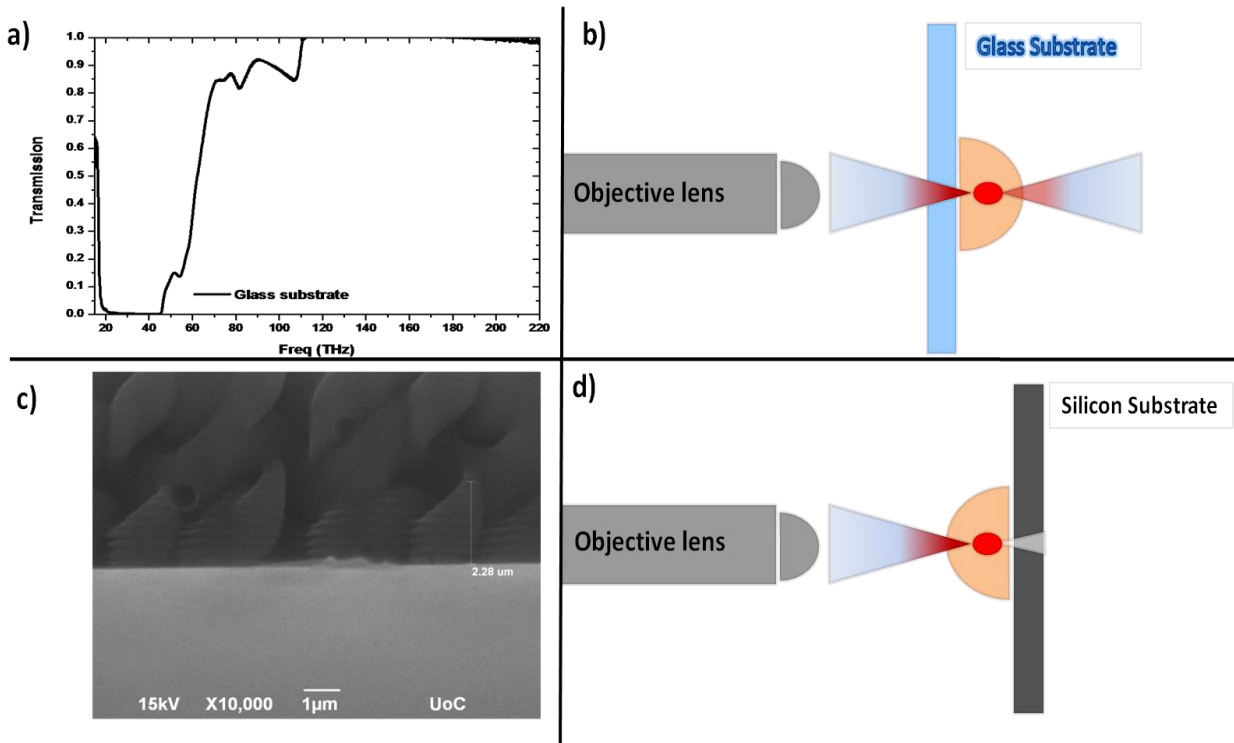


**Figure 11.** (a) Transmission spectra of glass in our interest range (20-80THz) shows clearly the unsuitability of this material for substrate. (b) Fabrication process takes place in normal way (the beam passes first through the substrate and then polymerizes the material). (c) SEM image of a structure in silicon substrate shows a waveform of the polymerize material near to the substrate (its cause of the reflection). (d) Writing process but this time the beam meets first the material, we can find the fabrication start position from the high reflection in the surface of silicon.

In our study we use silicon wafers from Graphene Supermarket, the diameter of the wafers was 100mm. Then we manage to cut in small round pieces approximately at 15mm diameter. An important point is the thickness of the wafer which is 525  $\mu\text{m}$  with the oxide thickness  $\sim 285\text{nm}$ . The resistivity of the silicon wafer is  $\rho = 10^{-3}$  to  $5 \cdot 10^{-3} \Omega\text{cm}$ . The structural orientation of the wafer is  $\langle 100 \rangle$ ; and finally, it is n-type semiconductor doped with Arsenic atoms.

Appealing, the silicon wafers are thicker comparing to the silicon oxides substrates but at the same time 55% more transparent. If we increase the thickness then as it is normal we decrease the transparency. One further exploration can be the introducing of substrates which are more elastic; in order to fabricate the structures on substrates we can be flexible. A huge capacity of applications demands elastic substrates and devices which can bend; and deserved further exploration.

### ***2.2.3 Material Synthesis***

The photo-structurable material employed in this study is hybrid organic-inorganic and we synthesize it in our lab. The components of the material can be monomers with organic and inorganic parts or inorganic molecules. Such materials have the advantage to combine different properties of the components in one nanoporous organic-inorganic matrix [19-23]. In order to synthesize our materials, the sol-gel process was used. The organic part combines monomer units which carry photo-structurable functional groups that are attached to the inorganic network. The ultraviolet (UV) photo-sensitivity of these materials arises from the use of photo-initiators. Such molecules, when exposed with specific wavelength radiation (usually UV light), have the ability of initiating polymerization of the organic part, resulting in the formation of an organic-inorganic network.

For the formation of the inorganic network Methacryloxypropyl Trimethoxysilane (MAPTMS) and Zirconium Propoxide were used. MAPTMS, 2-Dimethyl-amino-ethyl-Methacrylate (DMAEMA) served as the monomers. As photoinitiator, 4,4'-Bis(diethylamino) benzophenone (BIS) was used.

Figure 12 and 13 shows the chemical formulas and the reaction of the above molecules. First we mix MAPTMS (1,3031ml) with Hydrochlorium (0,1303ml), the latter component hydrolyze the MAPTMS. Thus, we produce hydrolyzed metal alkoxides or monomers; MAPTMS can provide trialkoxysilane functional group which attached to the inorganic network. The inorganic network it is important because keeps the polymeric structure with no or low shrinkage after the develop. The mixing of the two components takes place for 10 minutes under stirring in 20ml vial.

In one separate vial we add first the DMAEMA (0,3792ml) and then the Zirconium Propoxide (0,9957ml). It worth noting that, the Zirconium Propoxide is sensitive to the oxygen of the atmosphere, thus we add the Zirconium Propoxide drop by drop in the volume of DMAEMA. By that way the exposure time of the Zirconium Propoxide in oxygen is reduced as it is possible. The mix of the two components takes place under stirring for 10 more minutes.

The hydrolyzed MAPTMS was then added drop-wise to the ZPO solution, following another 20 minutes of stirring. It is important that the mixture should remain transparent. The mixture was stirred for 15 minutes, following the subsequent addition of a small amount of nanopure water (0,1891ml). The next step concerns the photoinitiator Bis (0,0166gr) which is in powder form, was added in the mixture under 25 minutes of continuous stirring. In order to avoid big clusters of not dilute components, especially from the photo-initiator the solution was filtered using 0.2  $\mu\text{m}$  syringe filters.

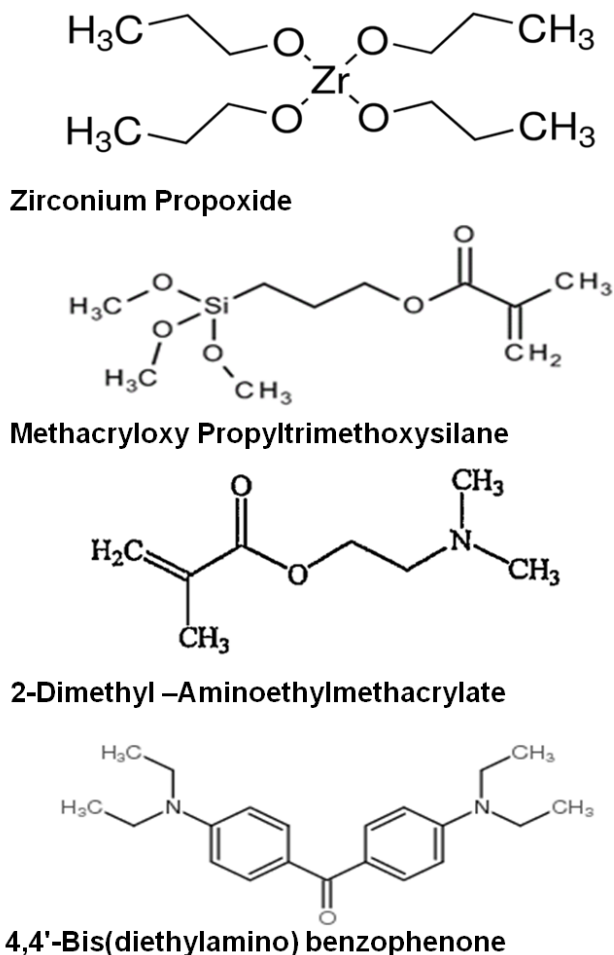
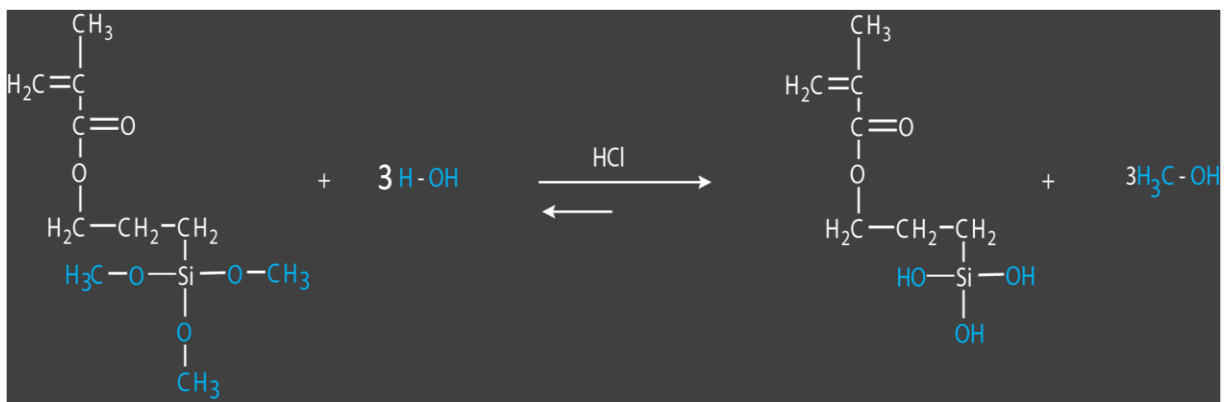


**Figure 12.** Chemical formulas of the precursor molecules used for the synthesis of the hybrid materials. From the top: Zirconium Propoxide, MAPTMS, DMAEMA and last the BIS

Finally, the samples were prepared by drop-casting onto thin glass or Silicon substrates, and the resultant drops were dried under vacuum at  $\sim 50^\circ\text{C}$  temperature for  $\sim 20$  hours before photopolymerization. We should be careful with the minimum thickness of the drops in order to avoid any reflections, thus we prefer to prepare drop at least 150nm thick. After the heating of

the samples the material transform to gel, thus it is more stable and provide the advantage for photo-fabrication with the sample placed upside-down to the piezoelectric stages.

All chemicals are from Sigma Aldrich and were used without further purification. Analytically one can see the synthesis procedure to [17-19]. The selection of the components of the material is important, its component has many advantages, e.g. DMAEMA is the molecule with metal binding affinity and plays great role to the metallization procedure, which we will discuss analytically to the next paragraphs.



*Hydrolysis of MAPTMS*

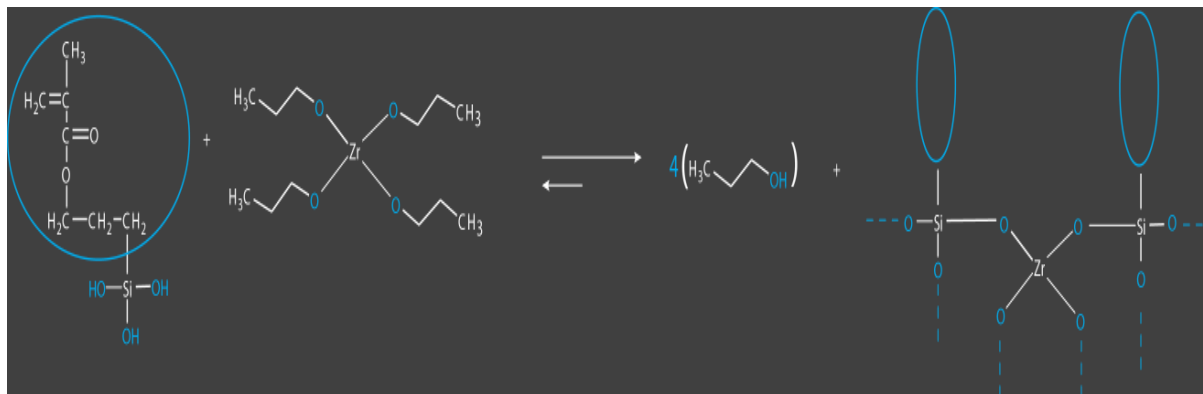


**Figure 13.** Chemical reactions leading to the Si-Zr composite. Fig(12,13) By Iakovos Gavalas Department of Material Science and Technology, University of Crete.

### **2.3 Metallization Process**

After the synthesis of our hybrid material which can change form from gel to solid after the polymerization procedure, one can see that we fabricate template dielectric materials, and the last step is the metallization process in order to obtain metallic nanostructures. The metallization process took place under two different procedures: Gold and silver coating.

Both procedures are ideal to metalize three dimensional polymeric structures with:

- Size greater than  $3 \times 3 \times 3 \mu\text{m}^3$  (total size of the structure, not the unit cell); in order to create a uniform layer of nanoparticles which is not comparable with the total height of the structure.
- The surface of the laser fabricated structures should contain free amino groups. The amino groups give the necessary selectivity for the metal coating.
- The mechanical and chemical stability of the polymeric templates should be high; and thus the structures remain stable with any deformation of shape, size and orientation after the multiple washes of the metallization procedures

#### **2.3.1 Gold metallization:**

##### **1st experimental procedure**

The methodology contains a sequence of sinking in solutions. At the beginning, the three dimensional structures to be metallized are let either into an aqueous 0.05 mol/l gold salt ( $\text{HAuCl}_4$ ) from Sigma-Aldrich for different residence times (hr): 20, 25, 30, 35, 40, and 45, in order to find the optimum immerse time. A critical point is that the amine groups (DMAEMA) of the hybrid material become protonated and positively charged, bounding, thus, electrostatically the metal species, acting actually as a metal trap for the metal ions.

After completion of this process, we take them out and we wash off the metal which does not take part in the metallization process with double distilled water. The cleaning procedure can be repeated twice or thrice depending on the morphology and the porosity of the structure. After, the specimens are subsequently dipped into an aqueous 6.6 M Sodium Borohydride ( $\text{NaBH}_4$ ) solution in order to reduce the metal ions and form metal nanoparticles. The above mentioned step is metal reduction step; so as to form the silver nanoparticles seeds on the three dimensional nanostructures.

It is during this step that the material surface gets fully covered with densely packed either gold nanoparticles allowing the selective plating of the structures. At this stage we explore the optimum conditions for reducing times, so we split its previous time into two samples of 20 & 25

hours remaining in solution. The table below describes the first and second step; the letters correspond to different final samples. Finally, the samples rinsed again for four times with double distilled water; as in the previous step, and were dried at room temperature under vacuum for ~ 18hours.

<b>HAuCl<sub>4</sub>(hr)</b>	<b>NaBH<sub>4</sub> (hr)</b>
<b>20</b>	<b>A:20</b>
	<b>B:25</b>
<b>25</b>	<b>C:20</b>
	<b>D:25</b>
<b>30</b>	<b>E:20</b>
	<b>F:25</b>
<b>35</b>	<b>E:20</b>
	<b>F:25</b>
<b>40</b>	<b>G:20</b>
	<b>H:25</b>
<b>45</b>	<b>I:20</b>
	<b>J:25</b>

The advantage of this procedure is that the nanoparticles that creates are small compared to others metallization processes which describes below. Thus, complex three dimensional metamaterial structures, such as helix, were allowed for metallization without any deformation of the polymer template. Sometimes the structures overloaded with nanoparticles; and lose the well defined structuring and periodicity. Thereby, the metallized structures cannot have the desired response. Unfortunately, the conductivity of this procedure is  $\sim 10^5$  S/m; one order of magnitude lower than the silver metallization [23,33]. Therefore, this protocol is ideal for metamaterials, meta-devices and photonic crystals which are resistant to lower conductivity values.

## 2nd experimental procedure

The procedure we followed is a variation of the procedure described in detail in [29], and employs two liquid gold solutions at the final plating step. The divergence lies in the fact that due to the polymeric nature of our scaffold, neither high temperature drying nor any use of hydrofluoric acid solution was used. A point of attention is that in our case we didn't apply



surface amine enrichment because the structures already have exposed amino groups (DMAEMA). Thus, the start position is the electroless gold deposition.

Analytically, we follow the protocol of the literature [29]. The gold deposition comprises three main steps, first the samples immersed into a solution of 0.16 M Sodium Borohydride ( $\text{NaBH}_4$ , Alfa Aesar, Ward Hill, MA, USA) with 60 vol% ethanol at room temperature, under continuous stirring (preferred in a plastic container) for 18 hours (in our case). Moreover, the samples rinsed three to four times with ethanol in aqueous solution 60 vol%. Next, were incubated with a mixture comprised of 0.16 M Sodium Borohydride ( $\text{NaBH}_4$ , Sigma Aldrich, Germany) with 60 vol% ethanol at room temperature. The reaction is very fast and should be completed within a few minutes (~10 min), the structures immersed again but this time with de-ionized water for three to four times, depending on the morphology of the polymeric template.

The final step includes immersing of the structures in a commercial electroless gold solution (Bright Electroless Gold, Transene Company, Inc., Danvers, MA, USA) which had been diluted by 50% in an aqueous solution of ethanol (60 vol%). A solution comprised of 0.16 M  $\text{NaBH}_4$  with 60 vol% of ethanol was then introduced under continuous stirring for maximum two minutes at room temperature. The solution at this point turned to black, something that makes the utilization of the structures more labored. The surface of the specimens then becomes colored (gold) after the addition of  $\text{NaBH}_4$ . In order to produce thicker metal coated structures we can leave the samples for longer time into the solution. Eventually, the samples rinsed again for four times with de-ionized water and once or two with anhydrous methanol (depending on the morphology of the polymeric template), the gold-coated specimens were dried at 50 °C (no more than 50 °C in order to preserve the form of the coated polymeric scaffolds) for 8-10 hours.

### **Juxtaposing the metallization techniques**

The above described metallization techniques were compared towards the determination of the optimum process which enables the conversion of the non-conductive polymeric scaffolds to conductive devices. Upon this changeover procedure, no distortion of shape, morphology and, especially in the case of metamaterials and photonic crystals; periodicity can be tolerated. Having this requirement in mind, the first presented technique exceeds clearly the second one in terms of the structures quality. In particular, by following the first experimental procedure, one can avoid the final step of plating, having the same results with the second technique. The advantage is that not only the metallization process takes place in shorter time but the number of the solutions into which the structures are immersed is reduced.

Eventually, the hallmark of the 1st prescription is that the metal ions have sufficient time to form enough electrostatic bonds with the unsheltered amino groups of DMAEMA. Therefore, during this step we can obtain the majority of the amino groups occupied with metal ions so that the subsequent step results to a layer uniformly decorated with metal nanoparticles. On the contrary, if we increase dwell time in the solution of  $\text{HAuCl}_4$  the outcome would be the opposite,

structures loaded more than normal. In this case the metallized structures lose the ability to imitate the original template.

### 2.3.2 Silver Metallization

The silver metallization of the 3D microstructures was a modification of the method reported by Kawata et al. [31]. For seeding, the samples were first immersed in a 0.05 mol/L  $\text{AgNO}_3$  solution at room temperature for 38-42 hours, and after rinsing with double distilled water, they were subsequently dipped into an aqueous sodium borohydride solution (6,6 M) to reduce the silver ions and form silver nanoparticles. This process was found to be sufficient and leads to fully covered film surface with densely packed silver nanoparticles allowing thus the selective silver plating of structures in the next step. The amount of silver nanoparticles onto the structures was found to be proportional to the immersion time in the solution of  $\text{AgNO}_3$  and sodium borohydride solution, and then the films turned out to be “mirror-like” only for the longer metal seed and reduction times.

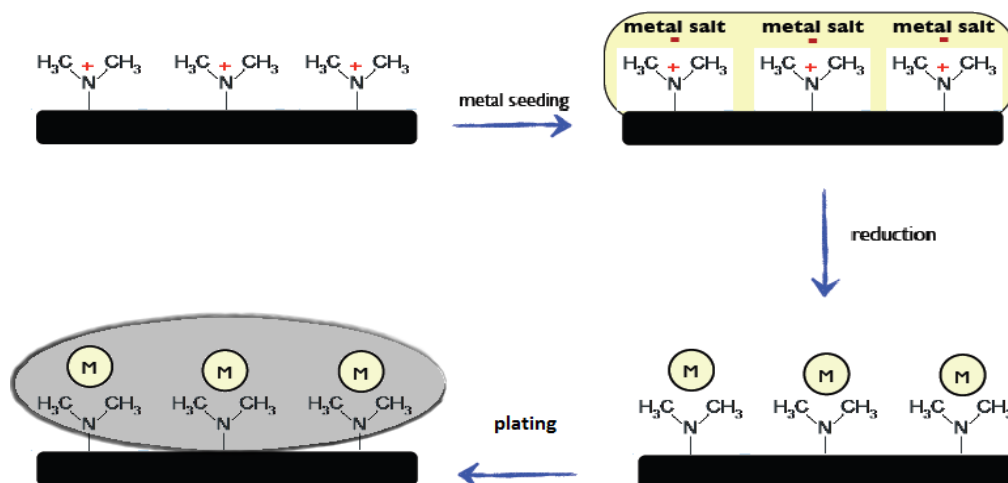


**Figure 15.** The graph demonstrates the role of DMAEMA. Electrostatic bonds are created between the polymer structure and the metal ions (silver/gold).

We mainly follow the steps of reference [23,33] for the synthesis and metallization process, however, not all the chemicals were the same. Nanopure water (double distilled and heated) was used in all experiments. The materials that used were silver nitrate ( $\text{AgNO}_3$ , 99%), sodium borohydride ( $\text{NaBH}_4$ , 99%), glucose ( $\text{C}_6\text{H}_{12}\text{O}_6$ ) and ammonia water ( $\text{NH}_3$ , 25%). For the seeding procedure we added 0.08493 gr of silver nitrate in 10 ml of nanopure water. We mix the samples in the solution and let them for 38-42 hours. In the reduction process, we create a solution of sodium borohydride with nanopure water (1.5 gr of  $\text{NaBH}_4$  in 16 ml). The time ranges between 20 and 24 hours.

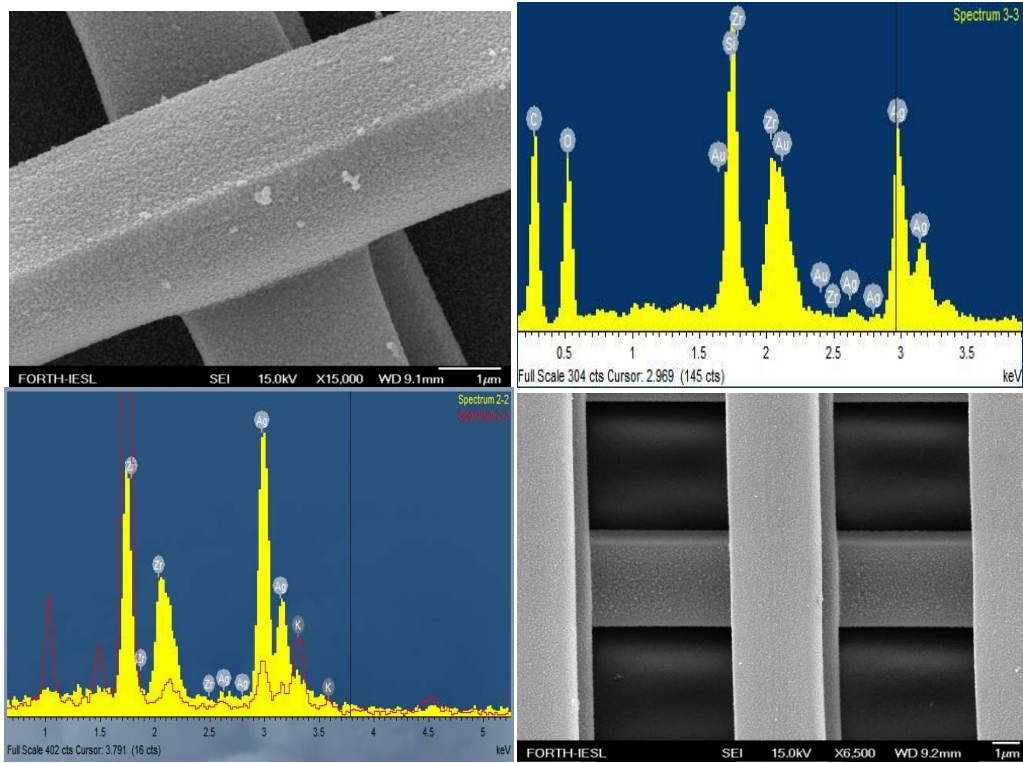


**Figure 16.** SEM pictures with the silver parts at the surface of the polymer material and Electron Dispersion X-ray (EDX) spectrum.

After the characterization by Scanning Electron Microscopy (SEM) and Dispersion Electron X-ray's (EDX) we are sure that the polymer scaffold is fully covered with silver nanoparticles. Finally, we achieve to fabricate conductive micrometer structures chemically and physically stable, and then we are ready for FT-IR characterization.

The conductivity of the structures strongly depends on the morphology and roughness of the metallized surface. In our case, the specimens loaded with gold or silver nanoparticles; and thus the surface is rough. One different approach, in order to transform the surface to smooth, is the thermal annealing of the metallized samples. The procedure that we proposed comprised two main steps; first, the rinsing for several times with de-ionized water and once with methanol of aqueous solution 50%, then gold-coated specimens were dried at 50 °C for five hours. Second, the thermal annealing procedure [24,25]; the samples placed in a furnace and heated at 200 °C for two hours. Then, the nanoparticles melt and create a uniform metal layer. Next, we decrease the temperature in the chamber 10 °C per minute, in order to avoid the creation of big clusters of metal.

Finally, the metal on the surface cools down and creates a uniform metallic layer, which is smoother compared with non annealing samples; and also enough thick compared to the skin depth  $\sim 20\text{nm}$  at THz frequency range. By that way we aim at increased conductivity values. This procedure not held in our study, but it is a promising processing to obtain metallic metamaterials structures and photonic crystals with high conductivity values. The conductivity of the annealing specimens is comparable with the conductivity of bulk materials (gold or silver  $\sim 10^7\text{S/m}$ ). As we will discuss analytically to the next chapter the experimental and simulated conductivities of the structures should be close. Otherwise, large diversion exists on the behavior of the structures; thus, comparison and convergence of the two would be impossible.

Summarizing, in this chapter was presented the synthesis, fabrication and metallization of the metamaterial structures. We began our consideration with the theory of two photon absorption and then we explore the two photon polymerization. In the latter mechanism based the technique which we use, the direct laser writing. Then we present the substrate selection; in order to obtain transparent substrates at the THz frequency region. Moreover, we illustrate the synthesis of the photosensitive material; which is a mixture of organic and inorganic components. After, we explore multiple metallization procedures. First, we introduce two electroless gold metallization processes. The first gold metallization protocol is suitable for the coating of complex three dimensional meta-devices; the synthesized nanoparticles are really small ( $\sim 5\text{-}10\text{nm}$ ) compared to second one ( $\sim 30\text{-}50\text{nm}$ ) [29]; and thus doesn't affect the shape of the polymeric template. Finally, we showed the improved protocol for silver metallization; which analytically discussed in the literatures [11,12,31].

The above mentioned procedure is ideal for coating structures bigger than  $3 \times 3 \times 3 \mu\text{m}^3$ , in order to create a uniform layer of nanoparticles which is not comparable with the total height of the structure. Otherwise, one can see that if the structures are smaller than the predicted dimensions then we have a foul loaded with silver nanoparticles specimens.

The next chapter discusses the final step of this study; which is the characterization of the laser fabricated and electroless metal coated structures. All the structures were allowed to dry for one day and then proceed to the characterization process. A point of attention is that the samples should maintain into dehumidifier; in order to avoid oxidation effects. The oxidation of the metal nanoparticles leads to decrease conductivity.

### ***3. Characterization of Metamaterials***

The experimental electromagnetic (EM) characterization of the direct laser writing fabricated photonic metamaterials discussed here was performed with both reflection and transmission measurements. The measurements were carried out using a Bruker Vertex 70v Fourier-transform infrared spectrometer with a collimated beam, attached to a Bruker Hyperion 2000 infrared microscope and two linear ZnSe grid polarizers. All the results of the measurements were successfully compared with corresponding reflection/transmission simulations.

In order to simulate electromagnetically our photonic infrared metamaterials we used a commercial three-dimensional full-wave solver (CST Microwave Studio, Computer Simulation Technology GmbH, Darmstadt, Germany) based on the finite element method.

#### ***3.1 Electromagnetic characterization of SCR system***

For the numerical characterization of the SCR structure we considered a single unit cell, as shown in Figure 4, with periodic boundary conditions along the x and y axes, while an incident plane wave propagating along the z-direction was used to excite the structure. For modeling the metallic parts of the structure (silver; yellow color in Figure 4) we considered a lossy-metal model with a conductivity  $\sigma_{Ag} = 5.71 \times 10^6$  S/m, in agreement with previous conductivity measurements [19,20].

##### ***3.1.1 Reflection Measurements***

The SCR structures were fabricated on silicon oxide substrate ( $\text{SiO}_2$ ); this kind of substrates are not transparent below 100 THz and therefore do not allow transmission measurements. That's why we experimentally characterized our structures by measuring only the reflection components. Figure 17 illustrates four reflection components which correspond to linearly polarized light ( $R_{xx}$ ,  $R_{xy}$ ,  $R_{yx}$  and  $R_{yy}$ ) where

the first and second lower indices indicate the output (reflected) and input signal polarizations, respectively [9,10].

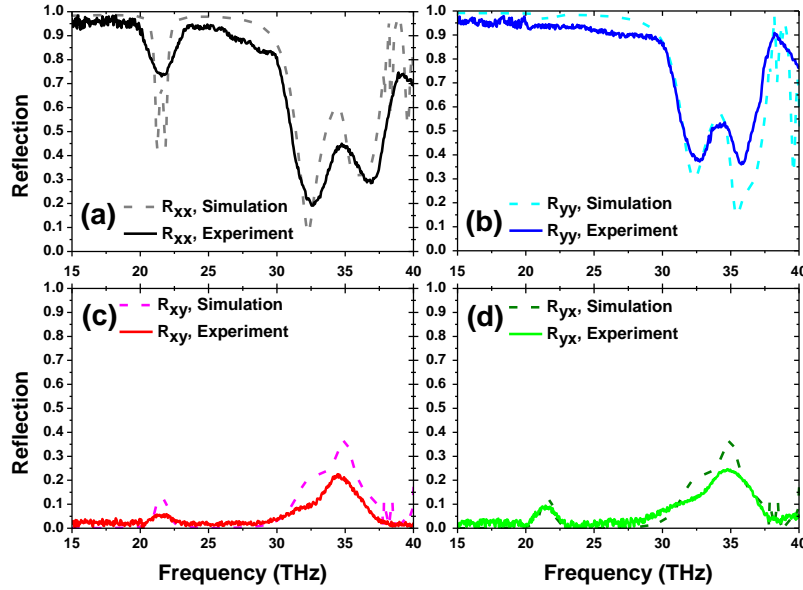


**Figure 17.** Dashed lines: Simulation and Solid lines: Experimental magnitude of the reflection components for the 3D SCR metamaterials under consideration and for a linearly polarized incident wave. All four reflection components, Rxx, Ryy, Rxy, and Ryx, can be seen in (a), (b), (c), and (d), respectively.

The good quality of the structures fabrication is reflected to the very good agreement between simulations (dashed lines) and experiments measurements (solid lines). Some differentiation is normal, resulting probably from sample roughness and imperfections as well as from the finite (along x-y) nature of the sample and the particle-like form of the metal that covers the DLW scaffold.

### 3.1.2 Transmission Properties: Asymmetric Transmission

In order to study wave propagation and transmission in anisotropic structures like the one discussed here, usually the transmission matrix is employed,  $T$ , which connects the transmitted with the incident fields as follows:

$$\begin{pmatrix} E_x^t \\ E_y^t \end{pmatrix} = \begin{pmatrix} T_{xx} & T_{xy} \\ T_{yx} & T_{yy} \end{pmatrix} \begin{pmatrix} E_x^i \\ E_y^i \end{pmatrix} \quad (1)$$

For an incident plane wave the matrix  $T$  above corresponds to propagation along the  $z$  axis. In Eq. (1)  $E_x^t, E_y^t$  denote the Cartesian components of the transmitted electric field, while the  $E_x^i, E_y^i$  those of the incident field. The *asymmetric transmission* is often characterized by the parameter  $\Delta$ . The parameter  $\Delta$  indicates the difference in transmittance of two waves propagating to opposite directions for example in our case the forward and backward  $z$ -direction, i.e,

$$\Delta = |T^f|^2 - |T^b|^2 \quad (2)$$

For reciprocal systems like the SCR structure [10], the matrix which connects the transmission matrix for the backward and forward direction according to the [9] is:

$$\begin{pmatrix} T_{xx}^b & T_{xy}^b \\ T_{yx}^b & T_{yy}^b \end{pmatrix} = \begin{pmatrix} T_{xx}^f & -T_{yx}^f \\ -T_{xy}^f & T_{yy}^f \end{pmatrix} \quad (3)$$

Thus, the asymmetric transmission for x-polarized incident wave is related to:

$$\Delta = \Delta^{(x)} = |T_{xx}^f|^2 + |T_{yx}^f|^2 - |T_{xx}^b|^2 - |T_{yx}^b|^2 = |T_{yx}^f|^2 - |T_{xy}^b|^2 \quad (4)$$

According to the above consideration similar equation exists for a y-polarized incident wave:

$$\Delta = \Delta^{(y)} = |T_{xy}^f|^2 + |T_{yy}^f|^2 - |T_{xy}^b|^2 - |T_{yy}^b|^2 = |T_{xy}^f|^2 - |T_{yx}^b|^2 = -\Delta^{(x)}$$

The last equation shows that for evaluating the asymmetric transmission for both forward and backward directions, it is equal to calculate the transmission, only for the forward direction for both x and y polarized incident waves. Figure 18 demonstrates the calculated four transmission components for our SCR structure, for x- and y-polarized incident waves.

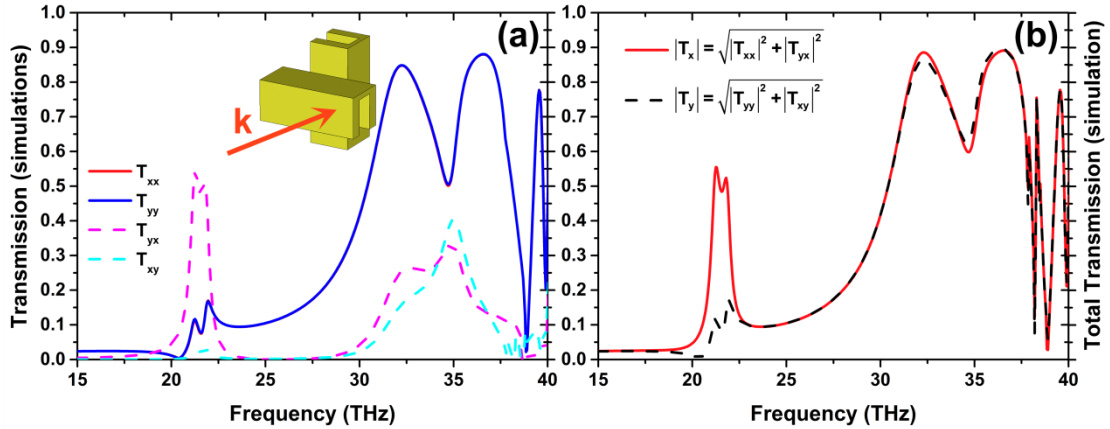


**Figure 18.** (a) Simulated transmission components (absolute values) for linearly polarized incident waves propagating through the 3D SCR structure along the forward (positive) z-direction. The red solid curve coincides with the blue solid curve. (b) Total transmitted amplitude for x- and y polarized incident wave,  $|T(x)^f|$  and  $|T(y)^f|$ , respectively, propagating in the forward z-direction. Note that for our structure  $|T(y)^f| = |T(x)^b|$ ; thus the asymmetric transmission response of the structure for an x-polarized incident wave is demonstrated.

In our case  $T_{xx}$  and  $T_{yy}$  are the same in all frequency regions; this can be concluding also by observing the symmetry of the structure. On the contrary, the cross polarized transmission amplitudes  $T_{yx}$  and  $T_{xy}$  are quite different especially in the region focused at 21 THz, reflecting a strong asymmetric transmission, which is highlighted better in Figure 19 where the parameter  $\Delta$  is plotted. There, black-dashed and red-

solid lines correspond to x and y linearly polarized incident waves propagating in the forward z direction.

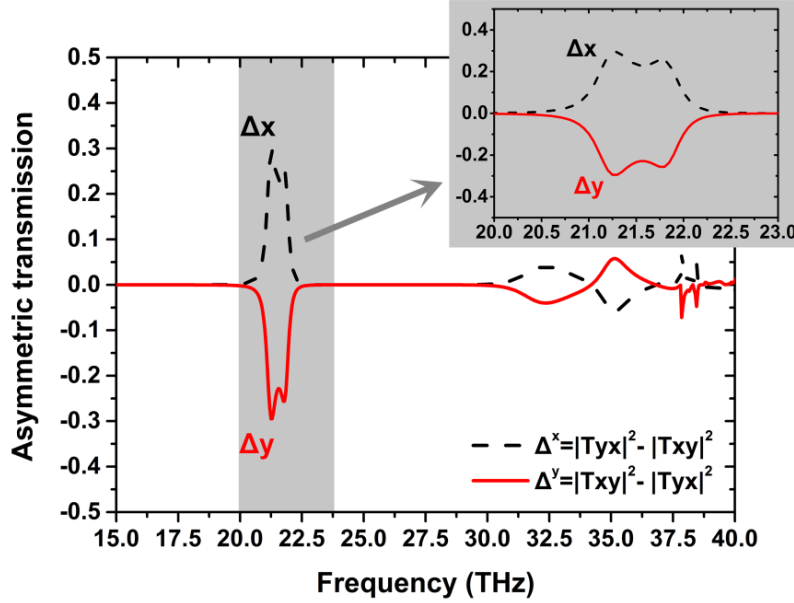


**Figure 19.** The asymmetry factor curves show a quite broad-band peak with asymmetric transmission close to 30%, centered at about 21.5 THz and two peaks of smaller asymmetric transmission, at around 32.5 THz, and 35.1 THz, correspondingly.

Where asymmetric transmission band at ~21THz comes from? Before 21 THz the structure behaves as a total reflector with its response dominated by the metallic cubes parallel to incident electric field, which respond as continuous wires. Thus, we have a wire grid polarizer and a stop-band before 21THz. When we approach 21THz strong magnetic field  $H_y$  is induced in the parallel to the incident magnetic field SCRs which induces a strong magnetic field  $H_x$  in the second SCRs (due to the physical connection of two), rising to give a y-polarized transmitted wave.

### 3.1.3 Polarization transformer response

The next analysis corresponds to the polarization characterization of the transmitted wave, through calculation of its ellipticity and orientation angle (optical activity). The results are shown in Figure 20, indicating at the asymmetric transmission band of 21THz ~90 degrees pure optical activity, i.e. optical activity associated with close to zero ellipticity of the transmitted wave. This means that a x polarized incident wave is almost totally transformed to y polarized wave when passing through the structure, maintain the linear polarization character. This validates the potential of our structure to be used as a 90 degrees one way polarization converter.



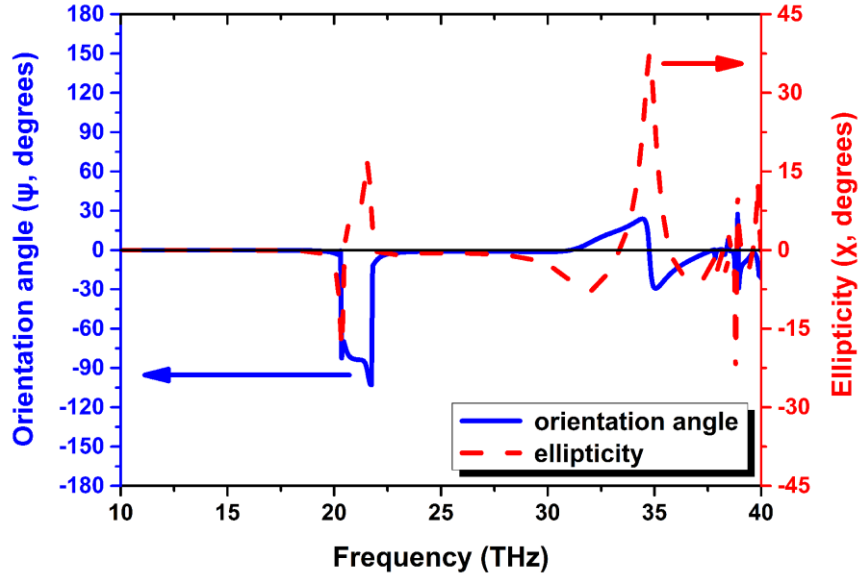


**Figure 20.** Simulated orientation angle,  $\psi$  (blue solid line), and ellipticity angle,  $\chi$  (red dashed line), for the 3D SCR metamaterial under consideration.

### 3.2 Helix Characterization

One different approach takes place in this part of the study; the fabrication of the helix in Si substrate. Si is quite transparent compared with  $\text{SiO}_2$  in THz region allowing the characterization of the structures via transmission instead of reflection measurements. The DLW gives us the advantage to fabricate quite complex structures with high spatial control in polymerization process, i.e. 3d helix (spirals in three directions), simple helix and gyroid geometries. It is important to note that the structures are fabricated with great mechanical properties and chemical stability.

#### 3.2.1 Scanning Electron Microscopy (SEM) Characterization

In this part of the work we demonstrate the fabricated simple helix and 3d helix structures. The morphology of the helix for both the simple and 3d geometries is shown in Fig. 21. We metalized with gold and silver nanoparticles the simple helix structure in order to explore the possibilities of different metals coating processing. Moreover, The electromagnetic response of the resulted structure was measured by Fourier transformation infrared spectrometry and the results were compared with corresponding simulation data.

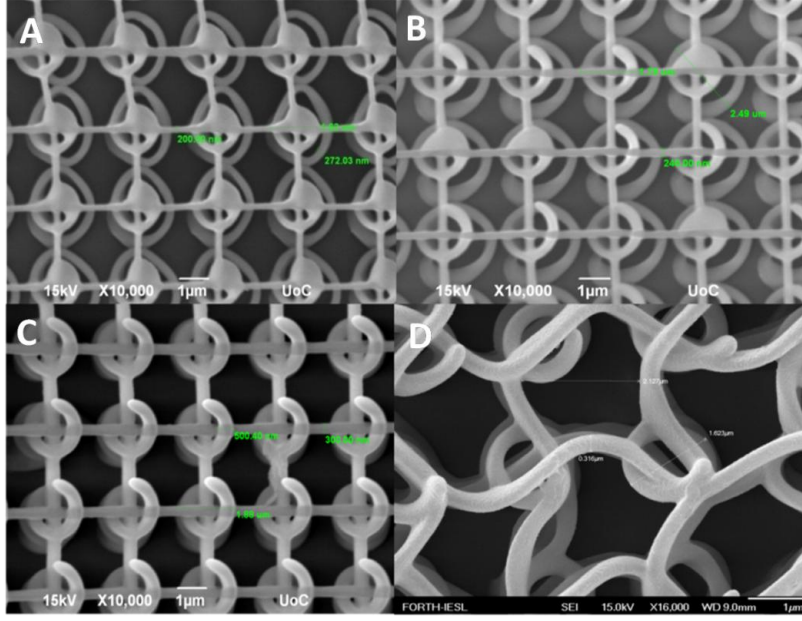


**Figure 11.** Scanning Electron Microscopy images for both helical structures. (A)-(C) Simple helix for different laser power. The thickness of polymer increases according to the increase of laser intensity, as it is expected. (D) 3d helix; such geometry may lead to phase separation and beam splitting effects, and deserves further exploration.

### 3.2.2 Linear Polarization Characterization

In order to check how accurate the protocols of metallization with silver and gold nanoparticles are, we measure transmission for linearly polarized light and we present the results in Figs. 22 and 23. The data concern all transmission components for linearly polarized incident waves:  $T_{xx}$ ,  $T_{xy}$ ,  $T_{yx}$  and  $T_{yy}$ . The transmitted field  $E^t$  is related to the incident field  $E^i$  via the transmission matrix [27,39] (Eq. (1)),

$$E_i^t = \overline{T}_{ij} E_j^i,$$

The subscripts  $i, j$  correspond to the plane of polarization,  $x$  or  $y$ , as we mentioned above for the SCR measurements.

Firstly, it is apparent from the graphs that the decrease of the conductivity leads to smoother and lower intensity curves; this is normal and expected consequence. Furthermore, Figure 22 and 23 present a stop band for all transmission amplitudes  $T_{xx}$ ,  $T_{xy}$ ,  $T_{yx}$  and  $T_{yy}$  for frequencies below 30 THz. Interestingly, the components  $T_{xx}$  and  $T_{yy}$  illustrate good agreement between simulations and experiment for frequencies lower than 40THz; above 40THz there is a deviation in case of silver helixes.

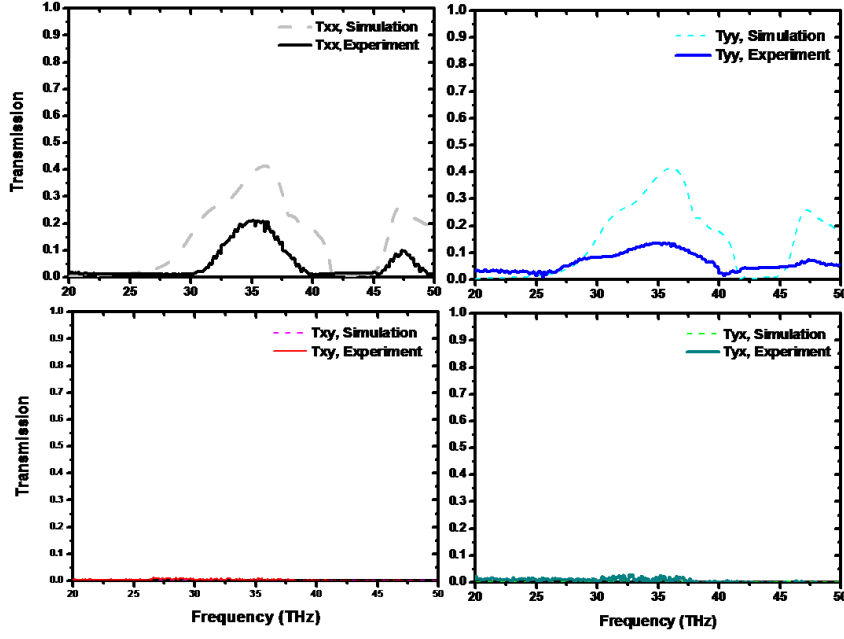


**Figure 22.** The figure presents the four transmission amplitudes  $|T_{xx}|$ ,  $|T_{yy}|$ ,  $|T_{xy}|$  and  $|T_{yx}|$  for the gold simple helix metamaterial shown in Fig. 5, for linearly polarized incident wave. The gold has been simulated using conductivity  $\sigma \sim 10^5 S/m$ . With dashed and solid lines are simulation and experiment, respectively.

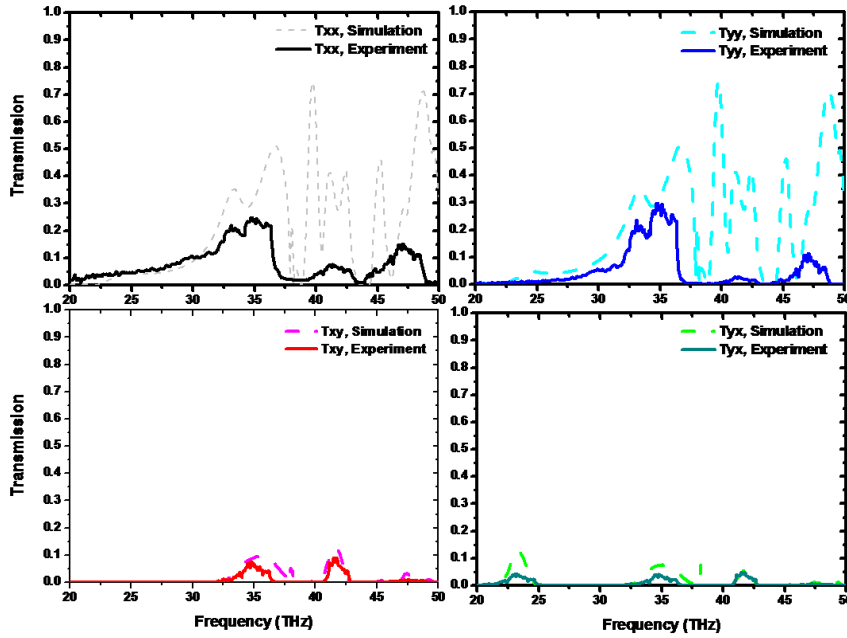


**Figure 23.** The graph presents all four transmission amplitudes for linearly polarized light for the silver helix-spiral structures. The silver has been simulated using conductivity  $\sigma \sim 10^6 S/m$ .

Possible reasons may be that the metallic surface is not so smooth as the metal which is considered in theory or the substrate shows more absorption than the one taken into

account in the simulations. Moreover, it is known that the metal nanoparticles oxidized by the oxygen of the atmosphere; by the procedure of oxidation the conductivity declines as it is normal. A scenario of oxidation is also possibly in our case. After the end of plating we keep the samples into dehumidifier but this is not enough; we can avoid the oxidation by using dehumidifier with nitrogen flow.

### 3.2.3 Response to circularly polarized incident wave

This chapter describes the data analysis. The analysis is based on the investigation of the transmission for circularly polarized waves. In our analysis we focus in the study and explanation of the polarization filtering effect by observing the magnetic field distribution.

#### Experimental Technique and Data Processing

For the study of our metallic helix metamaterials the circular transmission matrix  $T$ , defined by  $E_i^t = T_{ij}E_j^i$ , which describes the transmission properties for circularly polarized waves is of particular interest. Here  $i, j$  correspond to *Left-handed* (LCP, -) or *Right-handed* (RCP, +) circularly polarized waves, with the handedness defined as the electric field vector's direction of rotation at a fixed point in space, seen by an observer looking into the beam. The circular transmission matrix  $T$  can be calculated from the linear transmission matrix  $\bar{T}$  using the following basis transformation [16,17,24,25]:

$$\bar{T} = \begin{pmatrix} T_{++} & T_{+-} \\ T_{-+} & T_{--} \end{pmatrix} = \frac{1}{2} \times \begin{pmatrix} (T_{xx} + T_{yy}) + i(T_{xy} - T_{yx}) & (T_{xx} - T_{yy}) - i(T_{xy} + T_{yx}) \\ (T_{xx} - T_{yy}) + i(T_{xy} + T_{yx}) & (T_{xx} + T_{yy}) - i(T_{xy} - T_{yx}) \end{pmatrix} \quad (5)$$

Figure 24 shows the calculated spectra for the spiral geometry (two pitches). As can be seen there the extinction of the one of the two different polarizations is extremely high and recommends the structure for applications as broadband circular polarizer.

From Fig. 24 it can be seen also that the polarization filter response seems better in the case of the silver helix; this is expected due to higher conductivity. The structure though shows good polarization filtering properties for both gold and silver, which is a great advantage as it permits the application nature to decide for the metal coating.

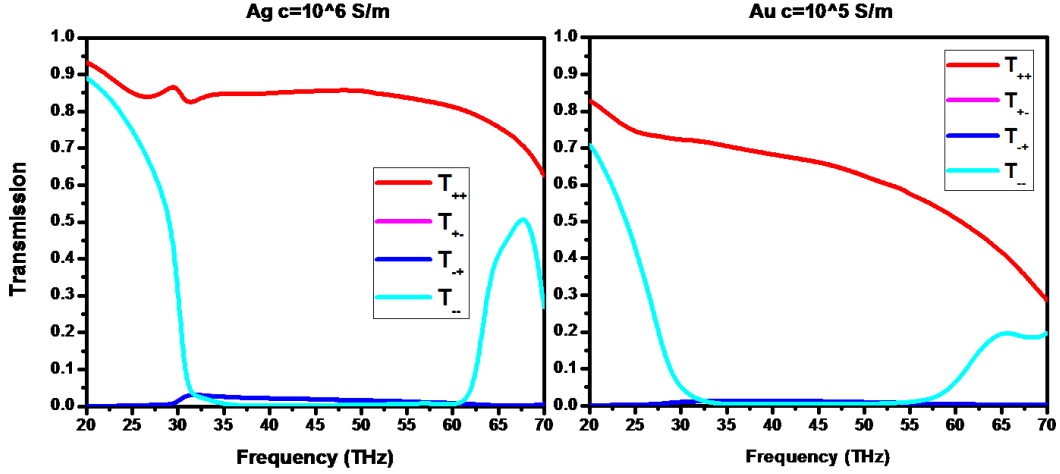


**Figure 24.** The All four transmission amplitudes (calculated) for circularly polarized light for both silver and gold metallized helical structures.

To examine the physical origin/mechanism of the above mentioned polarization filtering properties of the helix structure we examined the surface current distribution at 35.15 THz for the incident field configuration considered in Fig. 25. Fig. 26 shows the surface current along the helix for both left and right-handed circularly polarized incident wave. For LCP wave one can see that the current is restricted in the first pitch, resulting to strong reflected wave and not allowing transmission. This is not the case for RCP incident wave.

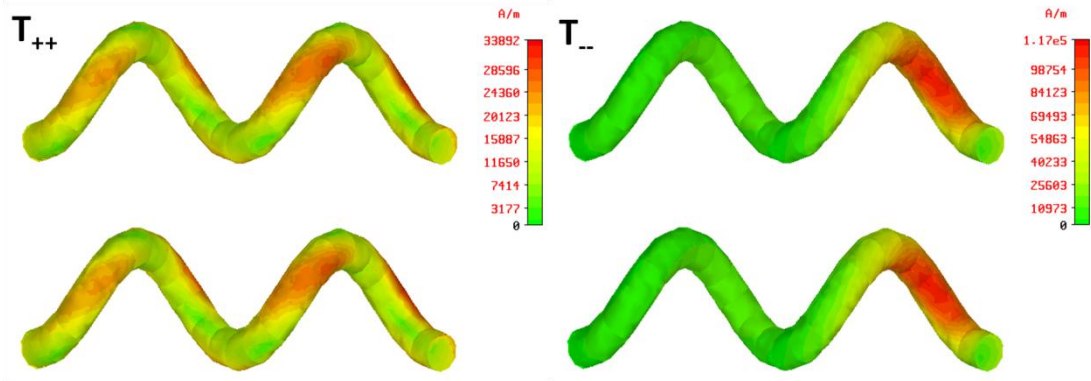


**Figure 25.** Magnitude of the surface current distribution in our helical structures at 35.15THz for both RCP (+) LCP (-) incident waves propagating along the axis of the helix.

#### ***4. Conclusion and Future Aspects:***

This thesis presents a systematical study, both theoretical and experimental, of the electromagnetic wave propagation characteristics of two different novel THz metamaterial structures fabricated by Direct Laser Writing. The first structure concerns a reciprocal metamaterial with strong electric and magnetic response; the results present interesting asymmetric transmission, almost 30%, and huge optical activity without significant ellipticity for linearly polarized light. These render the structure ideal for applications such as THz polarization rotators, filters and wave-plates.

The second structure is a spiral-type structure which shows interesting response to circularly polarized light. There we focused mainly on the exploration of new metallization procedures. Although the fabrication process is difficult, we managed to fabricate free standing, mechanically and chemically stable helices. Furthermore, we managed to metallize them with both gold and silver nanoparticles and we examined the dependence of the polarization control properties on different metal responses.

The investigation of such a rich variety of phenomena as the ones afore-mentioned is indication for plethora of possibilities for micrometer and nanometer scale metamaterials. Especially when such structures operate in so called "Terahertz Gap" [39] where there is a serious lack of electromagnetic wave manipulation components but a great potential in applications.

Next we present our recent work published in American Chemical Society (ACS) Photonics. The paper concerns the first structure (SCR's) which already discussed analytically. Moreover, we demonstrate the scaling down of the structure uniformly by a factor of 100; the afore mentioned consideration leads to asymmetric transmission and polarization control capabilities in the optical region.

## References

1. Kock, W. E. (1946). "Metal-Lens Antennas". IRE Proc. 34 (11): 828.
2. Veselago, V. G. (1968) "The electrodynamics of substances with simultaneously negative values of  $\epsilon$  and  $\mu$ ". Sov. Phys. Usp. 10 (4): 509–14.
3. J.B. Pendry, "Negative Refraction Makes a Perfect Lens". Phys. Rev. Lett. 85 (2000) 3966.
4. J.B. Pendry, D. Schurig, D.R. Smith, Science 312 (2006) 1780.
5. Pendry, John B.(2004). "Negative Refraction". Contemporary Physics (Princeton University Press) 45 (3): 191–202.
6. Economou E. "Solid State Physics. Vol. II: Order, Disorder, Correlations" Crete University Press, 2003
7. Gay-Balmaz, Philippe; Martin, Olivier J. F. (2002)."Electromagnetic resonances in individual and coupled split-ring resonators" Journal of Applied Physics 92 (5): 2929.
8. Shelby, RA; Smith, DR; Schultz, S (2001). "Experimental Verification of a Negative Index of Refraction". Science 292 (5514): 77–9
9. **G. Kenanakis, A. Xomalis, A. Selimis, M. Vamvakaki, M. Farsari, M. Kafesaki, C. M. Soukoulis, and E. N. Economou. "A three-dimensional infra-red metamaterial with asymmetric transmission". ACS Photonics 10.1021(2015).**
10. Bassiri et al. "Electromagnetic wave propagation through a dielectric–chiral interface and through a chiral slab". J. Opt. Soc. Am. A 1988, 5, 1450–1459.
11. N. Vasilantonakis, et. al. "Three-dimensional metallic photonic crystals with optical bandgaps, " Adv.Mater. 24 1101 (2012).
12. K. Terzaki, et. al. "3Dconducting nanostructures fabricated using direct laser writing". Opt. Mater. Express 1 586 (2011).
13. El-Kady et. al. "Direct Laser Writing of Graphene Electronics". ACS Nano, 2014, 8 (9), pp 8725–8729
14. Viskadourous et. al. "Direct laser writing of flexible graphene field emitters". Appl. Phys. Lett. 105, 203104 (2014)
15. Konios et. al. "Reduced Graphene Oxide Micromesh Electrodes for Large Area, Flexible, Organic Photovoltaic Devices". Advanced Functional Materials. 25. 15. 2213–2221 ( 2015)
16. Kymakis et. al. "Flexible Organic Photovoltaic Cells with In Situ Nonthermal Photoreduction of Spin-Coated Graphene Oxide Electrodes". Advanced Functional Materials. 23.21. 2742–2749 (2013)
17. Terzaki et. al. "Mineralized self-assembled peptides on 3d laser-made scaffolds: A new route toward 'scaffold on scaffold' hard tissue engineering" Biofabrication 5 (4), 045002. (2013)
18. Danilevicius et. al. "Burr-like, laser-made 3D microscaffolds for tissue spheroid encagement" Biointerphases. 10(2):021011 (2015)

19. Chatzinikolaïdou, et. al "Adhesion and growth of human bone marrow mesenchymal stem cells on precise-geometry 3D organic–inorganic composite scaffolds for bone repair". *Materials Science and Engineering: C*, 48 301-309. (2015)
20. Skarmoutsou, et. al. "Nanomechanical properties of hybrid coatings for bone tissue engineering". *J. Mech. Behav. Biomed. Mater.* 25, 48-62. (2013)
21. Maria Farsari et.al. "Materials processing: Two-photon fabrication". *Nat. Photonics* 3, 450 – 452, (2009).
22. M. Farsari et.al "Multiphoton polymerization of hybrid materials". *Journal of Optics*, 12, 124001, (2010).
23. Ovsianikov et al. "Ultra-Low Shrinkage Hybrid Photosensitive Material for Two-Photon Polymerization Micro-fabrication". *ACS Nano*, 2, 2257-2262, (2008).
24. Bechelany M. et. al. "Synthesis Mechanisms of Organized Gold Nanoparticles: Influence of Annealing Temperature and Atmosphere". *Crystal Growth Design*, 10.2. 587–596 (2010).
25. Lin J. et. al. "Growth of Solid and Hollow Gold Particles through the Thermal Annealing of Nanoscale Patterned Thin Films". *ACS Applied Materials Interfaces*. 5.22.11590–11596 (2013).
26. Kang, M et. al. "Asymmetric transmission for linearly polarized electromagnetic radiation". *Opt. Express* 2011, 19, 8347–8356.
27. Mutlu, et. al."Asymmetric transmission of linearly polarized waves and polarization angle dependent wave rotation using a chiral metamaterial". *Opt. Express* 2011, 19, 14290–14299.
28. S. Linden et. al. "Magnetic Response of Metamaterials at 100 Terahertz". *Science* (2004) vol. 306 no. 5700 pp. 1351-1353
29. Fang Y., et. al. "Biologically Enabled Syntheses of Freestanding Metallic Structures Possessing Sub-wavelength Pore Arrays for Extraordinary (Surface Plasmon-Mediated) Infrared Transmission". *Adv. Funct. Mater.* 2012, 22, 2550–2559
30. Gansel et.al. "Gold Helix Photonic Metamaterial as Broadband Circular Polarizer". *Science* (2009) Vol. 325 no. 5947 pp. 1513-1515
31. Zhang, Y. S. et.al. "Negative Refractive Index in Chiral Metamaterials" *Physical Review Letters*. 102, 023901 (2009).
32. Na Liu et. al. "Stereometamaterials". *Nature Photonics* (2009) 3, 157 – 162
33. S. Kawata et. al. "Fabrication of 3D metal/polymer microstructures by site-selective metal coating". *Appl. Phys.A* (2007).. 90(2), 205–209
34. Menzel, et. al. "Advanced Jones calculus for the classification of periodic metamaterials". *Phys. Rev. A* 2010, 82, 053811.
35. G. Kenanakis, et. al. "Optically controllable THz chiral metamaterials". *Opt. Express* 22, 12149 (2014).
36. J. Zhou, et. al., "Negative refractive index due to chirality". *Phys. Rev. B* 79(12), 121104 (2009)



37. Kriegler et. al., "Bianisotropic Photonic Metamaterials". IEEE Journal of selected topics in quantum electronics, vol. 16, No. 2.(2010)
38. C. M. Soukoulis et. al. "Negative index materials: New frontiers in optics". Advanced Materials 18, pp. 1941-1952 (2006).
39. R. Singh, et. al. "Terahertz metamaterial with asymmetric transmission", Phys. Rev. B 80, 153104 (2009)

**Published work:**

**A three-dimensional infra-red metamaterial with asymmetric transmission**  
G. Kenanakis,<sup>1,\*</sup> A. Xomalis,<sup>1,2</sup> A. Selimis,<sup>1</sup> M. Vamvakaki,<sup>1,2</sup> M. Farsari,<sup>1</sup> M.  
Kafesaki,<sup>1,2</sup> C. M. Soukoulis,<sup>1,3</sup> and E. N. Economou<sup>1</sup>

<sup>1</sup> *Institute of Electronic Structure and Laser, Foundation for Research & Technology-Hellas, N. Plastira 100, 70013, Heraklion, Crete, Greece*

<sup>2</sup> *Department of Materials Science and Technology, University of Crete, 710 03 Heraklion, Crete, Greece*

<sup>3</sup> *Ames Laboratory-USDOE, and Department of Physics and Astronomy, Iowa State University, Ames, 50011 Iowa*

\*gkenanak@iesl.forth.gr

**Abstract**

A novel three-dimensional (3D) metallic metamaterial structure with asymmetric transmission for linear polarization is demonstrated in the infra-red spectral region. The structure was fabricated by direct laser writing and selective electroless silver coating, a straightforward, novel technique producing mechanically and chemically stable 3D photonic structures. The structure unit cell is composed of a pair of conductively coupled magnetic resonators and the asymmetric transmission response results from interplay of electric and magnetic responses; this equips the structure with almost total opaqueness along one propagation direction versus satisfying transparency along the opposite one. It also offers easily adjustable impedance, 90° one way pure optical activity and backward propagation possibility, resulting thus to unique capabilities in polarization control and isolation applications. We show also that scaling down the structure can make it capable to exhibit its asymmetric transmission and its polarization capabilities in the optical region.

**Keywords:** Metamaterials; Chiral media; Split-cube resonators; Asymmetric transmission; Direct laser writing.

**Introduction**

Electromagnetic Metamaterials (MMs) are artificial complex materials, composed of subwavelength-scale building blocks and having electromagnetic (EM) properties beyond anything that can be found in nature; these properties are due mainly to the geometric structure of the MM building blocks (often called “meta-atoms”), and less due to their constituent materials. Adjusting properly the MMs geometrical features, one can achieve properties such as negative refractive index, magnetism at optical frequencies, perfect absorption, enhanced optical nonlinearities, etc. Driven by those properties, several applications of two- dimensional (2D) and three-dimensional (3D) metamaterials have been proposed, including sub-wavelength resolution imaging

systems, compact polarization control elements, cloaking devices, filters, absorbers, sensors and biosensors<sup>1-5</sup>.

An unusual and counter-intuitive phenomenon that becomes possible with metamaterials and has attracted recently considerable attention is that of asymmetric transmission (AT), i.e. of different transmission of a polarized wave if sent by the two opposite sides of a metamaterial slab. This diode-like response, which originates from the different wave-structure coupling if the wave incidents from the two opposite sides of the slab, does not violate Lorenz' reciprocity theorem, and can find use in many EM wave manipulation devices such as polarization rotators<sup>6</sup>, isolators and circulators<sup>7</sup>.

The possibility of asymmetric transmission in reciprocal structures was discussed first in the context of two-dimensional (2D) planar chiral metamaterials, where asymmetric transmission for circularly polarized waves was observed<sup>8-11</sup>. This asymmetric transmission originates from the fact that an incident circularly polarized wave sees different handedness for the two opposite propagation directions. Many 2D planar metamaterials with asymmetric transmission for circularly polarized waves have been proposed and discussed in the literature, including microwave and THz chiral structures<sup>8, 9, 12</sup>, chiral plasmonic metamolecules<sup>13</sup> and general anisotropic 2D structures<sup>14</sup>. These structures though, due to their 2D character which implies mirror symmetry along the normal to their plane (propagation) direction, do not show asymmetric transmission for linearly polarized waves<sup>10</sup>, restricting thus the possibilities of the asymmetric transmission effect in applications.

To achieve asymmetric transmission for linearly polarized waves one needs to break the mirror symmetry also along propagation direction, avoiding simultaneously any C4 rotational symmetry in the structure plane (considering it normal to the propagation direction)<sup>15</sup>. Recently, employing such anisotropic metamolecules, various metamaterial structures showing asymmetric transmission for linearly polarized waves have been proposed and demonstrated, and the conditions relating asymmetric transmission and structure asymmetries have been discussed in detail<sup>15-19</sup>.

Most of the AT structures demonstrated to-date are structures based on the planar bi-layer conductor configuration, i.e. the unit cell is formed by a pair of planar conductors, electromagnetically coupled; transmission asymmetry originates from the asymmetric coupling of electric dipolar resonant modes of the two planar conductors. Despite the ease of fabrication, using such planar structures limit the possibilities offered by fully three-dimensional (3D) volumetric structures, which allow much larger variety of structure designs, allowing much more subwavelength scale metamaterial resonators and larger flexibility in the coupling between adjacent resonators-not only electromagnetic coupling but coupling via electric-current connections is allowed. Moreover, they allow asymmetric transmission to be

generated due to asymmetric coupling of magnetic rather than electric dipole resonances.

The involvement of magnetic resonators, besides electric resonators, in the AT effect offers the potential to adjust at will the structure impedance, matching for example the free space impedance and achieving higher transmission values. Moreover, it offers the potential to combine AT with backwards propagation, allowing e.g. backwards propagation along the one direction versus forward propagation at the opposite direction, leading to peculiar structure response.

In this work we demonstrate asymmetric transmission *generated by magnetic resonance coupling* in a *3D volumetric structure* based on two perpendicular split-cube resonators (SCRs) - see Fig. 1. The structure was fabricated by direct laser writing (DLW)<sup>20, 21</sup> and selective silver coating<sup>22, 23</sup>, a technique able to provide fully 3D structures with deep-subwavelength resolution. It operates in middle infra-red (15-40 THz), a frequency region of significant technological interest, where the requirement for EM wave control components is still high, despite substantial recent developments. Our structure, which exhibits asymmetric transmission for linear polarization only (and not for circular), while it is quite transparent along the one propagation direction, shows almost total isolation along the opposite direction, providing unique possibilities in polarization isolation applications. To achieve such an isolation response (zero vs high transmission), both the electric and magnetic response of the split-cube resonator components of the structure were exploited. This involvement of both electric and magnetic resonances equips the structure also with the possibility of one-way 90° pure optical activity offering additional capabilities for the control of the light polarization<sup>4, 24</sup>.

In what follows we present the structure design (Section 2), the fabrication (Section 3, detailed in Supplementary Material), and the methods employed to analyze the electromagnetic response of the structure, both theoretically and experimentally (Section 4). In Section 5 we present the results of the electromagnetic characterization of the structure, which include reflection measurements and simulations combined with transmission simulation and analysis, followed by a detailed discussion of our structure capabilities. Finally, in Section 6 we discuss a miniaturized, nm-scale version of the structure, which offers optical (at 750 nm wavelength) asymmetric transmission for linearly polarized light. The paper ends with our conclusions.

## The design

The unit cell of the 3D metamaterial design employed in the present study is shown in Fig. 1. It consists of two split-cube resonator (SCR) structures rotated by 90° with respect to each other along the  $z$ - (propagation) direction. The geometrical structure parameters for the structure as fabricated and characterized experimentally are detailed in the caption of Fig. 1.

As can be seen, the structure lacks mirror symmetry along all  $x$ ,  $y$ ,  $z$  directions as well as  $C_4$  rotational symmetry in the  $x$ - $y$  plane. It consists of two conductively coupled identical magnetic resonators with the back one (along  $z$ ) rotated  $90^\circ$  in respect to the front one. According to literature,<sup>17, 18</sup> structures of this symmetry are expected to allow asymmetric transmission for linearly polarized waves only. This comes from asymmetric cross-polarization conversion of a linearly polarized wave incident on the two opposite sides of the slab (along  $z$ -direction) and depends strongly on the polarization of the incident wave in the  $x$ - $y$  plane.

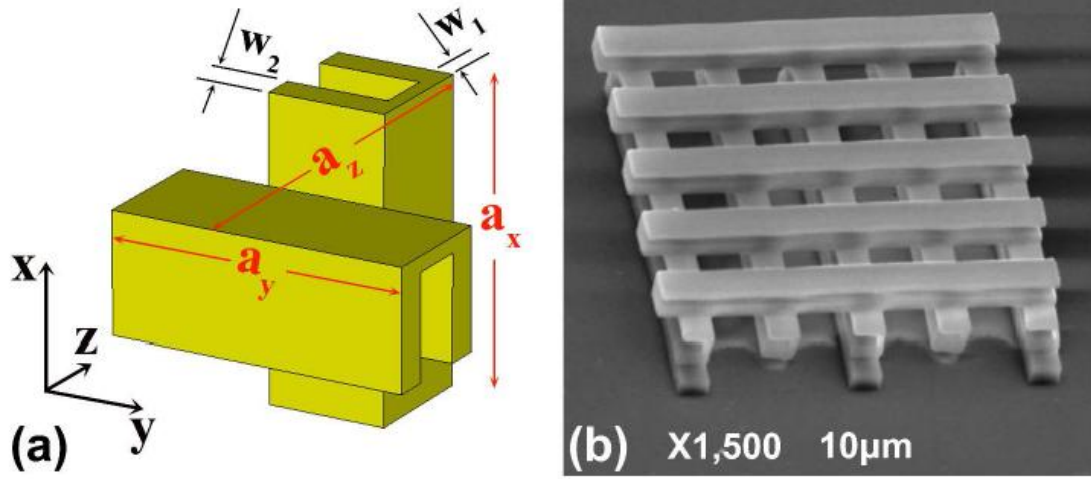


**Fig. 1:** (a) Schematic of the unit cell of the 3D SCR metamaterials under consideration. The dimensions of the fabricated structure are  $a_x = a_y = 8.0 \mu\text{m}$ ,  $a_z = 9.1 \mu\text{m}$ ,  $w_1 = 600 \text{ nm}$ , and  $w_2 = 850 \text{ nm}$ , respectively. The wave propagation is along the  $z$  direction. (b) Top view of SEM image of the 3D SCR metamaterials under consideration, recorded at 15 kVolts. The magnification scale can be seen below the SEM image.

### Structure fabrication

As was mentioned in the introduction, our structure was fabricated by Direct Laser Writing (DLW) followed by electroless silver plating. DLW by multi-photon polymerization is a 3D printing technology that allows the fabrication of 3D structures with resolution below 100 nm. Briefly, the beam of an ultra-fast laser is tightly focused inside the volume of a transparent and photosensitive monomer, causing it to absorb two or more photons and polymerize locally. By moving the beam in three dimensions inside the photopolymer volume, one can fabricate 3D structures of great accuracy. The photosensitive material used for the fabrication is an organic-inorganic composite, produced by the addition of Methacryloxypropyl Trimethoxysilane (MAPTMS) to Zirconium n-Propoxide. 2-(dimethylamino)ethyl methacrylate (DMAEMA), acting as a metal-binding moiety, was also added and copolymerized with MAPTMS upon photopolymerization. Michler's ketone (4,4-bis(diethylamino) benzophenone, BIS) was used as the photoinitiator. Further information on the fabrication technique and the photosensitive material synthesis can be found in the Supplementary section.

## Electromagnetic characterization

The experimental EM characterization of the structure discussed here was performed in the frequency region 15-40 THz, through reflection measurements, performed using a Bruker Vertex 70v Fourier-transform infrared spectrometer with a collimated beam, attached to a Bruker Hyperion 2000 infrared microscope and two linear ZnSe grid polarizers.

The results of the measurements were compared in all cases with corresponding reflection simulations. For these, we used a commercial three-dimensional full-wave solver (CST Microwave Studio, Computer Simulation Technology GmbH, Darmstadt, Germany) based on the Finite Element Method. We considered in the simulations a single unit cell, as shown in Fig. 1, with periodic boundary conditions along  $x$  and  $y$  directions, while an incident plane wave propagating along  $z$ -direction was used to excite the structure. For modeling the metallic parts of the structure (silver; yellow color in Fig. 1) considered a lossy-metal model with a conductivity of  $\sigma_{Ag}=5.71 \times 10^6$  S/m, in agreement with previous conductivity measurements <sup>22</sup>.

## Results and discussion

### *Reflection measurements*

Since the 3D SCR structure was fabricated on glass, which is not transparent in the far infrared region of interest, we characterized the structure experimentally by measuring the reflection rather than the transmission coefficients. The transmission coefficients were concluded indirectly, through simulations. Thus, for linearly polarized incident wave four reflection components were measured:  $R$ , where is the incident  $y$ -polarized electric field and is the reflected  $x$ -polarized electric field  $R_{xx}$ ,  $R_{xy}$ ,  $R_{yx}$  and  $R_{yy}$ , where the first and second lower indices indicate the output and input signal polarizations, respectively, e.g.  $R_{xy} = E_x^r / E_y^i$ , where  $E_y^i$  is the incident  $y$ -polarized electric field and  $E_x^r$  is the reflected  $x$ -polarized electric field <sup>25</sup>.

In Figures 2(a)-(d) we present both the experimental (solid lines) and the simulated (dashed lines) co-polarized and cross-polarized reflection amplitudes ( $|R_{xx}|$ ,  $|R_{yy}|$  and  $|R_{xy}|$ ,  $|R_{yx}|$  respectively) for the 3D SCR structure under consideration. One can observe in Figs. 2 the very good quantitative agreement between simulations and experiments, indicating the very good quality of the fabrication of the samples (slight disagreements in few cases are probably due to the better resolution in the simulation compared to the experiment, and to the slight sample roughness and imperfections; this is the origin also of the not-well resolved experimentally double dip of simulated  $R_{xx}$  around 21.5 THz – the double character of the dip is due to the coupling (leading to splitting) of the magnetic resonant modes of the two SCRs of the unit cell, as we will discussed latter). This very good agreement between simulations and experiments also allows us to base the subsequent calculations and analysis to the simulation results.

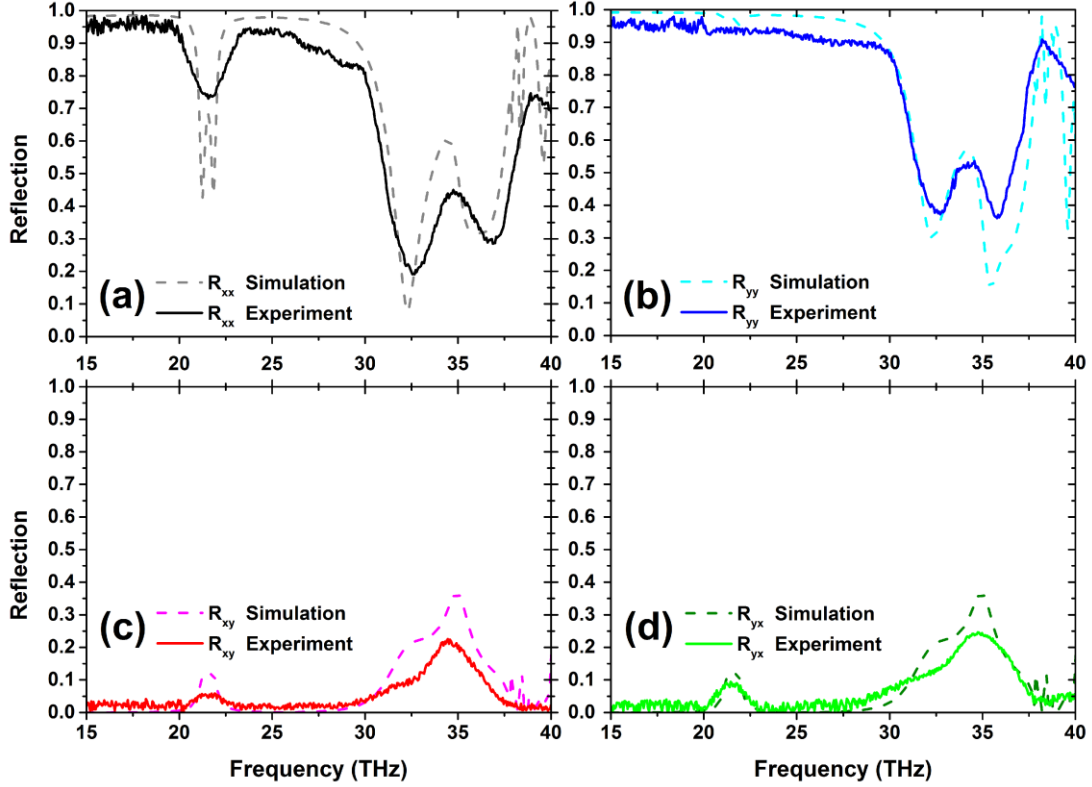


**Fig. 2:** Simulated (dashed lines) and measured (solid lines) *magnitude* of the reflection components for the 3D SCR metamaterials under consideration and for linearly polarized incident wave. All four reflection components,  $R_{xx}$ ,  $R_{yy}$ ,  $R_{xy}$  and  $R_{yx}$ , can be seen in Fig. 2(a), Fig. 2(b), Fig. 2(c) and Fig. 2(d), respectively.

#### *Transmission properties – Asymmetric transmission*

In order to study wave propagation and transmission in anisotropic structures like the one discussed here, usually the transmission matrix is employed,  $\vec{T}$ , which connects the transmitted with the incident fields as follows:

$$\begin{pmatrix} E_x^t \\ E_y^t \end{pmatrix} = \begin{pmatrix} T_{xx} & T_{xy} \\ T_{yx} & T_{yy} \end{pmatrix} \begin{pmatrix} E_x^i \\ E_y^i \end{pmatrix} \quad (1)$$

In Eq. (1) propagation of an incident plane wave along z-direction is considered and  $E_x^t, E_y^t$  denote the x and y component of the transmitted electric field, respectively.

By definition, asymmetric transmission, often symbolized as  $\Delta$ , is the difference in the transmittance (transmitted intensity divided by the incident intensity) for waves propagating along two opposite directions (in our case the forward (positive) and backward (negative) z-direction), i.e.

$$\Delta = |T^f|^2 - |T^b|^2 \quad (2)$$

With  $|\mathbf{T}|^2 = |\mathbf{E}^t|^2 / |\mathbf{E}^i|^2 = (|E_x^t|^2 + |E_y^t|^2) / |\mathbf{E}^i|^2$ , and the superscripts  $f$  and  $b$  denote the forward and backward  $z$ -direction respectively.

Let us consider the incident wave to be a linearly polarized wave polarized along  $x$ -direction, i.e.  $E_y^i = 0$ . The transmitted wave then will have in general both  $x$  and  $y$  components and the normalized transmitted intensity will be  $|\mathbf{T}|^2 = |\mathbf{T}_{(x)}|^2 = |\mathbf{T}_{xx}|^2 + |\mathbf{T}_{yx}|^2$ . (For a  $y$ -polarized incident wave it will be  $|\mathbf{T}|^2 = |\mathbf{T}_{(y)}|^2 = |\mathbf{T}_{yy}|^2 + |\mathbf{T}_{xy}|^2$ ).

In systems containing only reciprocal materials, as the one studied here, the transmission matrix for the backward propagation direction is connected to the transmission matrix for the forward direction as follows<sup>15</sup>.

$$\begin{pmatrix} T_{xx}^b & T_{xy}^b \\ T_{yx}^b & T_{yy}^b \end{pmatrix} = \begin{pmatrix} T_{xx}^f & -T_{yx}^f \\ -T_{xy}^f & T_{yy}^f \end{pmatrix} \quad (3)$$

Thus, the asymmetric transmission for a  $x$ -polarized incident wave becomes

$$\Delta = \Delta^{(x)} = |T_{xx}^f|^2 + |T_{yx}^f|^2 - |T_{xx}^b|^2 - |T_{yx}^b|^2 = |T_{yx}^f|^2 - |T_{xy}^f|^2. \quad (4)$$

(For a  $y$ -polarized incident wave,  $\Delta = \Delta^{(y)} = |T_{xy}^f|^2 + |T_{yy}^f|^2 - |T_{xy}^b|^2 - |T_{yy}^b|^2 = |T_{xy}^f|^2 - |T_{yx}^f|^2 = -\Delta^{(x)}$ .)

Eq. (4) shows that, in the case of reciprocal systems, asymmetric transmission is in fact asymmetric cross-polarization conversion between two perpendicular incident wave polarizations. This shows that to evaluate the asymmetric transmission instead of performing a transmission/reflection experiment (or simulation) for two opposite propagation directions one can realize the experiment/simulation only for the forward direction and for both  $x$ - and  $y$ -polarized incident waves.

Following this approach, in Fig. 3(a) we present the simulated transmission components  $T_{xx}$ ,  $T_{yy}$ ,  $T_{xy}$ ,  $T_{yx}$  (absolute values) for waves propagating along the positive  $z$ -direction in the 3D SCR structure; in Fig. 3(b) we show the total transmitted field amplitude for  $x$  and  $y$  incident wave polarizations,  $|\mathbf{T}_{(x)}|^2 = (|\mathbf{T}_{xx}|^2 + |\mathbf{T}_{yx}|^2)^{1/2}$  and  $|\mathbf{T}_{(y)}|^2 = (|\mathbf{T}_{yy}|^2 + |\mathbf{T}_{xy}|^2)^{1/2}$ , respectively. As can be seen in Fig. 3(a) in our case  $T_{xx} = T_{yy}$  in all frequency regions; this can be concluded also by observing the symmetry of the structure. On the other hand the cross-polarized transmission amplitudes  $T_{yx}$  and  $T_{xy}$  are quite different, especially in the region centered at 21.5 THz, indicating strong asymmetric transmission. This strong asymmetric transmission for frequencies between 21 and 22 THz is demonstrated clearly in Fig. 3(b) where the total transmission is shown (note that due to the equality of co-polarized transmission amplitudes  $T_{xx}$  and  $T_{yy}$  the total transmission for a  $y$ -



polarized incident wave propagating along the positive  $z$ -direction is equal to the total transmission of a  $x$ -polarized incident wave propagating in the negative  $z$ -direction, i.e.  $|T_{(y)}^f|^2 = |T_{(x)}^b|^2$ ). The strong asymmetric transmission of the structure is highlighted further in Fig. 4, where the parameter  $\Delta$  is plotted, according to Eq. (4).

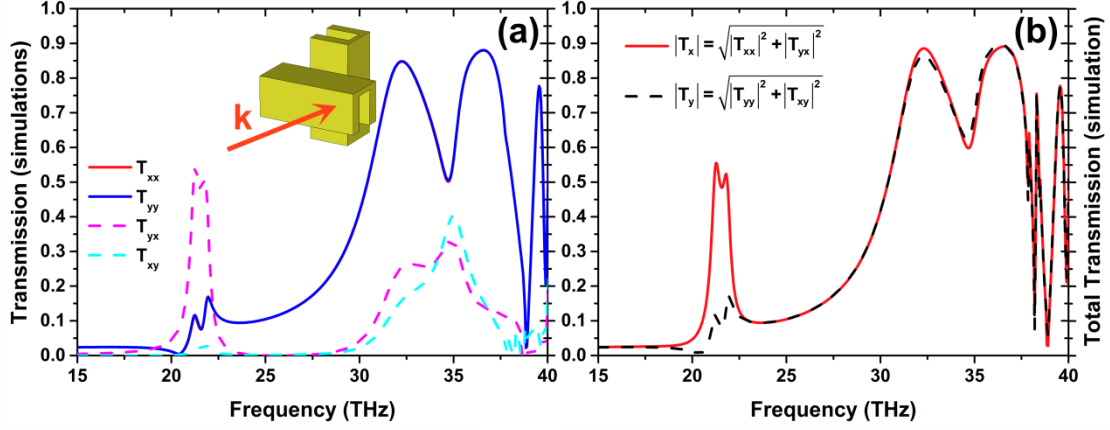


**Fig. 3:** (a): Simulated transmission components (absolute values) for linearly polarized incident waves propagating through the 3D SCR structure along the forward (positive)  $z$ -direction. The red solid curve coincides with the blue solid curve. (b): Total transmitted amplitude for  $x$ - and  $y$ -polarized incident wave,  $|T_{(x)}^f|$  and  $|T_{(y)}^f|$  respectively, propagating in the forward  $z$ -direction. Note that for our structure  $|T_{(y)}^f| = |T_{(x)}^b|$  thus the asymmetric transmission response of the structure for a  $x$ -polarized incident wave is demonstrated.

Observing the results of Fig. 3(b) one should note that, contrary to most of the structures discussed so-far in the literature, the asymmetric transmission band here at around 21.5 THz appears as pass-band imposed in a broad region of forbidden propagation and transmission (from zero to ~28 THz). This broad stop-band is due to a negative permittivity response provided by the metallic cubes which are parallel to the incident electric field direction (the metallic cubes act as a wire-grid-polarizer), resulting to small co-polarized transmission amplitudes  $|T_{xx}|$  and  $|T_{yy}|$ , as shown in Fig. 3(a). The transmission band around 21.5 THz (i.e. the asymmetric transmission band) is due to a magnetic resonance of the parallel to the external magnetic field cubes, coupled to the equivalent magnetic resonance of the perpendicular cubes, and superimposed to the negative permittivity response of the cubes, as we will demonstrate later on. (The double-peak character of that band is a result of the mode-splitting due to this magnetic resonance coupling.)

From the results of Fig. 3(b) one can see also that in the asymmetric transmission band around 21.5 the structure looks quite transparent along one propagation direction and quite opaque if “seen” from the opposite direction (for a linearly polarized wave polarized along one of the principal lattice directions). This “zero” versus “large” transmittance (which results from the large difference between  $|T_{xy}|$  and  $|T_{yx}|$  combined with the small values of the co-polarized transmission amplitudes  $|T_{xx}|$  and  $|T_{yy}|$ <sup>26</sup>) is a highly desired feature in polarization control applications.

As was mentioned also earlier, from the results of Fig. 3(a) one can notice that for our structure,  $T_{xx} = T_{yy}$ . This results in the asymmetric transmission occurring for only linearly polarized waves, while the transmission for circularly polarized incident waves is fully symmetric, as shown in literature<sup>15,17</sup>. The asymmetric transmission for linearly polarized waves in this case is a function of the polarization angle,  $\varphi$ ,

according to the relation  $\Delta^{(x)} = (|T_{yx}^f|^2 - |T_{xy}^f|^2) \cos(2\varphi)$ <sup>15</sup>.

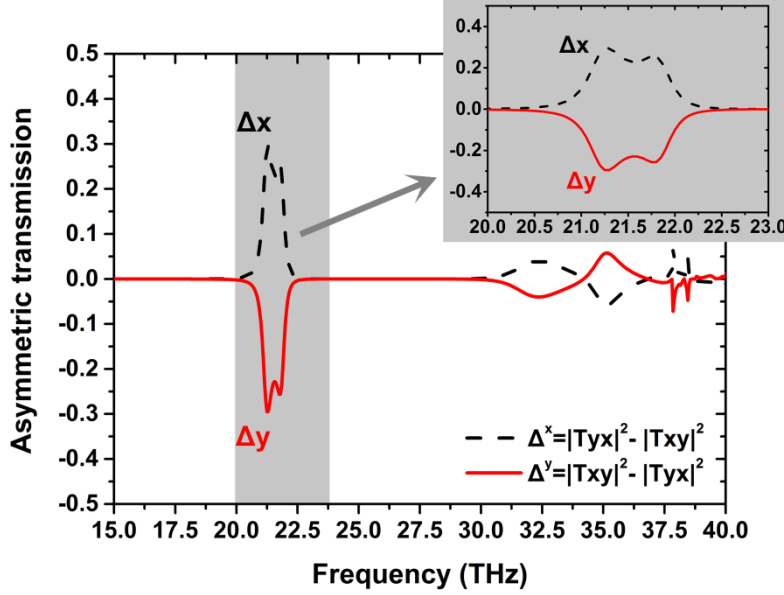


**Fig. 4:** Simulated AT parameter  $\Delta$  for the 3D SCR metamaterial under consideration. Black dashed and red solid lines correspond to AT of  $x$ - and  $y$ - linearly polarized incident waves propagating in the forward  $z$ -direction. The asymmetry factor curves show a quite broad-band peak with asymmetric transmission close to 30%, centered at about 21.5 THz (see inset), and two peaks of smaller asymmetric transmission, at around 32.5 THz, and 35.1 THz, respectively.

The asymmetric transmission response of our structure can be also indicated, but not definitively concluded, from the reflection measurements and simulations presented in Fig. 2. Taking into account that due to the symmetry of the structure  $|\mathbf{T}_{(x)}^b|^2 = |\mathbf{T}_{(y)}^f|^2$  and  $|\mathbf{R}_{(x)}^b|^2 = |\mathbf{R}_{(y)}^f|^2$ , where  $|\mathbf{R}_{(y)}^f|^2$  ( $|\mathbf{R}_{(x)}^b|^2$ ) is the reflectance of a forward (backward) propagating incident wave polarized along  $y$ -direction ( $x$ -direction), and  $|\mathbf{R}_{(x)}|^2 = |R_{xx}|^2 + |R_{yx}|^2$ ,  $|\mathbf{R}_{(y)}|^2 = |R_{yy}|^2 + |R_{xy}|^2$  (see Fig. 2 for the reflection components), one can see that in the absence of absorption the asymmetric transmission formula of Eq. (4) can become  $\Delta^{(x)} = |T_{yx}|^2 - |T_{xy}|^2 = |R_{yy}|^2 - |R_{xx}|^2$  (here the superscripts  $f, b$  have been omitted for simplicity, since the formula is valid for both forward and backward incidence directions), i.e. the asymmetric transmission can be expressed also through reflection amplitudes. This expression though is based on the fact that  $|\mathbf{R}|^2 + |\mathbf{T}|^2 = 1$  and it is not valid in the presence of absorption. However, for small absorption, a significant difference in the reflection amplitudes  $|R_{xx}|$  and  $|R_{yy}|$ , as in the case of Fig. 2 in the frequency region around 21.5 THz, can be considered as a signature of asymmetric transmission. (Note that the

equality of the cross-polarized reflection amplitudes  $|R_{xy}|$  and  $|R_{yx}|$ , which was assumed above, is a direct result of reciprocity and the structure symmetry<sup>27</sup>.

#### *Asymmetric transmission origin*

To investigate the origin of AT band at ~21.5 THz, we examined the field distribution in this spectral region. An example is shown in Fig. 5(b) where we plot the magnetic field amplitude at 21.5 THz for the incident field configuration shown in Fig. 5(a). The dominant magnetic field direction in the SCRs is indicated with arrows in Fig. 5(b).

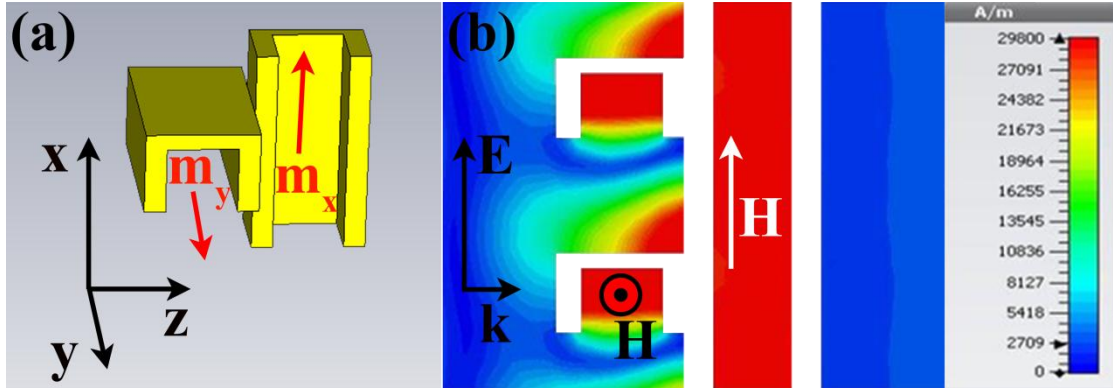


**Fig. 5:** (a): Unit cell of the 3D SCR metamaterials with the incident EM field considered.  $\mathbf{m}_x$  and  $\mathbf{m}_y$  are the resonant magnetic moments induced in the SCRs; (b) the total magnetic field amplitude in two unit cells (along  $\mathbf{E}$  direction) of the structure under consideration. The dominant direction of this field is shown with arrows.

Observing the fields (both amplitudes and phases) for the configuration of Fig. 5(a) (i.e. for a  $x$ -polarized incident field) one can see that below 21 THz the structure behaves as total reflector, with its response dominated by the metallic cubes parallel to the electric field, which behave as continuous wires<sup>28, 29</sup>. Approaching 21 THz, a strong magnetic field  $H_y$  is induced in the parallel to the incident magnetic field SCRs, which induces a strong magnetic field  $H_x$  in the second (perpendicular) SCRs (due to the physical connection, i.e. the conductive coupling, of the two SCRs), giving rise to a  $y$ -polarized transmitted wave. In other words, the incident magnetic field (along  $y$ -direction) excites circulating currents creating a resonant magnetic dipole moment  $\mathbf{m}_y$  in the first SCR; these currents, due to the physical connection of the two SCRs, lead to a potential difference between the two parallel to  $x$ - $y$  plane sides of the second SCR, and this difference is compensated with circulating current creating a magnetic moment  $\mathbf{m}_x$  at the second SCR, and providing thus cross-polarization conversion. This coupling is different in magnitude if the wave propagates towards the opposite (negative  $z$ ) direction (note that in the opposite direction to excite the parallel to the incident magnetic field cubes the incident wave has to “penetrate” a grid of metallic cubes parallel to its electric field – also the generated cross-polarized wave in order to be transmitted needs to “penetrate” a metal cube grid parallel to its electric field; the result is much smaller transmitted intensity). The magnetic resonance origin of the

transmission at  $\sim 21.5$  THz is confirmed also from the fact that the 21.5 THz frequency almost coincides with the magnetic resonance frequency of a single SCR.

The asymmetric transmission band at  $\sim 21.5$  THz implies a combination of magnetic resonance with electric response of wires-like systems, making our SCR system analogous to combined split-ring-resonator and wires systems, extensively discussed in previous literature<sup>29</sup>. This analogy suggests some important capabilities of our SCR system<sup>29</sup>: (a) by modifying the cross-section of the SCRs and/or the size of the unit cell one can greatly tune the structure impedance, matching that to the impedance of free space and achieving the highest possible asymmetric transmission through the structure; (b) by modifying the structure one can combine electric and magnetic responses in such a way as to achieve backward propagation in the asymmetric transmission band, realizing thus one-way backward asymmetric transmission components.

#### Polarization transformer response

Analyzing further the response of our structure at the AT band at  $\sim 21.5$  THz by examining the transmission matrix components shown in Fig. 3(a), one can see that a x-polarized incident wave is almost totally transformed to y-polarized wave when passing through the structure. This indicates a close to  $90^\circ$  “one-way” optical activity of the structure. To confirm this response we calculated the ellipticity and the optical activity for an x-polarized incident wave transmitted through the structure along the positive z-direction. For the calculation, we followed the approach of Ref.<sup>29</sup>; the details are discussed in the Supplementary Material section. The results are shown in Fig. 6, indicating at the asymmetric transmission band more than  $90^\circ$  pure optical activity, i.e. optical activity associated with close to zero ellipticity of the transmitted wave. This validates the potential of our structure to be used as a  $90^\circ$  one way polarization converter.

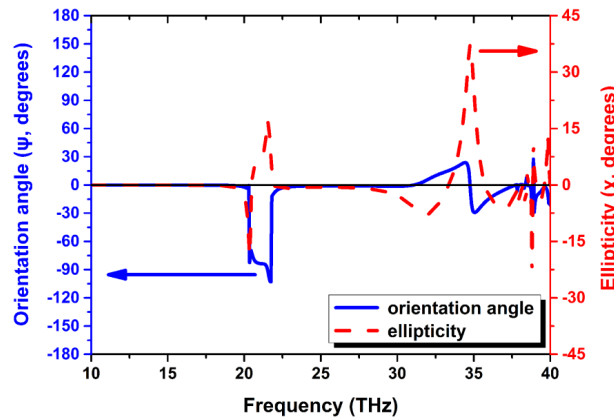


**Fig. 6:** Simulated orientation angle,  $\psi$  (blue solid line), and ellipticity angle,  $\chi$  (red dashed line) of the polarization ellipse for the wave transmitted through the 3D SCR metamaterials under consideration, when the metamaterial is excited by a x-polarized incident wave propagating along the forward z-direction.

### Nanometer-scale SCR structure

The asymmetric transmission and the resulting polarization control capabilities of the proposed here SCR design prompted us to examine the possibility to apply and exploit the same design also in the optical region. As has been shown quite recently though<sup>30, 31</sup>, the high losses and the large kinetic inductance of the metals in the optical region result to non-scalability of the magnetic resonance response of magnetic metamaterials with the structure size; in particular they lead to weakening and frequency saturation of the magnetic resonance in nanoscale magnetic metamaterials as the present SCR structure. Despite that, as we show here, the asymmetric transmission properties and capabilities of the proposed design can be also achieved and exploited in the optical region. The weakening of the magnetic response and the modification of the electric response of the structure (due to the change in the metal response from IR to visible) result, besides higher losses, to alteration of the structure impedance making it better matched to the free space impedance and thus beneficial for the AT response.

Scaling down the design of Fig. 1 uniformly by a factor of 100 and calculating the asymmetric transmission response of the resulting structure one achieves the results shown in Fig. 7. Fig. 7(a) shows the transmission amplitudes for a linearly polarized incident wave polarized along  $x$ - and  $y$ - direction while Fig. 7(b) shows the asymmetric transmission parameter  $\Delta$ , obtained through Eq. (4). Observing the results of Fig. 7, one can see that the asymmetric transmission here is even larger than the one of the similar infrared structure (compare Fig. 7(b) with Fig. 4) despite the larger losses of the metal in the optical region. This larger transmission is a result of the above mentioned better impedance match of the structure with its environment, associated with smaller reflectance. (A related slight disadvantage is the larger co-polarized transmittance which degrades the “zero” vs “large” transmittance picture which we discussed in Section 5.2). The results of Fig. 7 show the possibility to transfer and exploit our structure potential and functionalities also in the optical region, despite the non-size-scalability of magnetic metamaterial response up to this region (implying also that the strength of the magnetic response is not always essential for significant asymmetric transmission achievement).

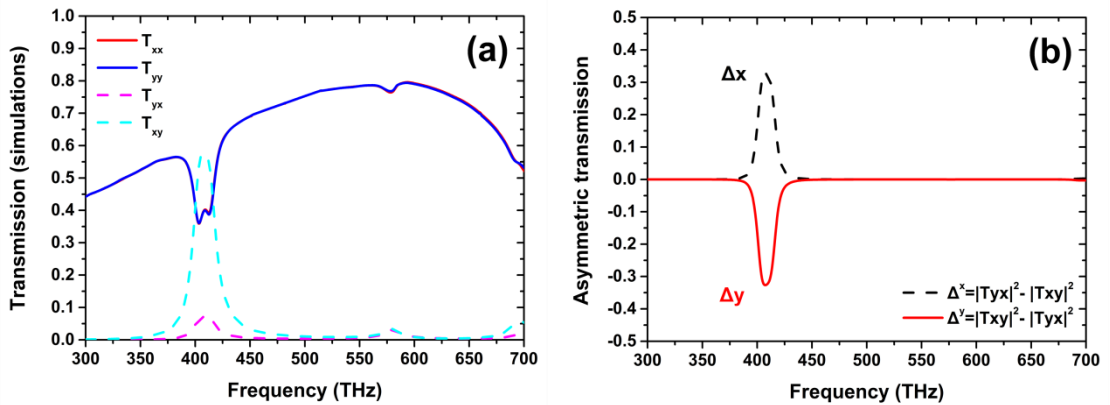


**Fig. 7:** Simulated magnitude of the linearly polarized transmission components (a), and simulated asymmetric transmission parameter  $\Delta$  (b) for the 3D SCR metamaterial shown in Fig. 1 scaled down uniformly by a factor of 100. The silver in this case is simulated using the data by P.B. Johnson and R.W. Christy<sup>32</sup>.

## Conclusions

We studied theoretically and experimentally the asymmetric transmission properties and the polarization control capabilities of a novel 3D infra-red metamaterial structure obtained by employing direct laser writing and selective silver coating. The structure is composed of two layers of split-cube-resonators (SCRs), mutually twisted by  $90^\circ$ . The experimental study was done through reflection measurements while associated transmission and reflection simulations revealed quite large asymmetric transmission for linearly polarized waves, zero versus quite large transmittance if the structure is “seen” from two opposite directions, and  $90^\circ$  one way pure optical activity. The achievement of these nice asymmetric-transmission-related properties of the structure is due to the combination of both electric and magnetic responses of the SCRs, and offers additionally the possibility of impedance control (adjusting thus the asymmetric transmission values), and of “one-way” backward propagation. Finally we showed that the nice asymmetric transmission properties of the structure can be transferred and exploited also in the optical region by uniformly scaling the structure unit cell.

In summary, the present study showed that this type of three-dimensional asymmetric transmission structures as the one discussed here which involve both magnetic and electric resonators offer unique capabilities in polarization control, something that makes them significant candidates for polarization manipulation components in optics.

## Acknowledgments

This work was supported by Greek GSRT project ERC02-EXEL and the 3DSET THALIS Program of the Hellenic Ministry of Education (MIS380278). Work at Ames Laboratory was partially supported by the Department of Energy (Basic Energy Sciences, Division of Materials Sciences and Engineering) under Contract No. DE-AC02-07CH11358 (computational studies).

**Supporting Information Available.** Detailed information about the structure fabrication, structural characterization and polarization transformer response. This information is available free of charge via the Internet at <http://pubs.acs.org/photronics>.

## References

- (1) Veselago, V. G., The electrodynamics of substances with simultaneously negative values of  $\epsilon$  and  $\mu$ . *Sov. Phys. Usp.* **1968**, *10*, 509-514.
- (2) Smith, D. R.; Pendry, J. B.; Wiltshire, M. C. K., Metamaterials and negative refractive index. *Science* **2004**, *305*, 788-792.
- (3) Soukoulis, C. M.; Wegener, M., Past achievements and future challenges in the development of three-dimensional photonic metamaterials. *Nat. Photonics* **2011**, *5*, 523-530.
- (4) Gansel, J. K.; Thiel, M.; Rill, M. S.; Decker, M.; Bade, K.; Saile, V.; von Freymann, G.; Linden, S.; Wegener, M., Gold helix photonic metamaterial as broadband circular polarizer. *Science* **2009**, *325*, 1513-1515.
- (5) Kabashin, A. V.; Evans, P.; Pastkovsky, S.; Hendren, W.; Wurtz, G. A.; Atkinson, R.; Pollard, R.; Podolskiy, V. A.; Zayats, A. V., Plasmonic nanorod metamaterials for biosensing. *Nat. Mater.* **2009**, *8*, 867-871.
- (6) Leung, D. M. H.; Rahman, B. M. A.; Grattan, K. T. V., Numerical analysis of asymmetric silicon nanowire waveguide as compact polarization rotator. *IEEE Photonics J.* **2011**, *3*, 381-389.
- (7) Hogan, C. L., The ferromagnetic faraday effect at microwave frequencies and its applications. *Reviews of Modern Physics* **1953**, *25*, 253-263.
- (8) Fedotov, V. A.; Mladyonov, P. L.; Prosvirnin, S. L.; Rogacheva, A. V.; Chen, Y.; Zheludev, N. I., Asymmetric propagation of electromagnetic waves through a planar chiral structure. *Phys. Rev. Lett.* **2006**, *97* (16), 167401.
- (9) Plum, E.; Fedotov, V. A.; Zheludev, N. I., Planar metamaterial with transmission and reflection that depend on the direction of incidence. *Appl. Phys. Lett.* **2009**, *94*, 131901.
- (10) Menzel, C.; Helgert, C.; Rockstuhl, C.; Kley, E. B.; Tunnermann, A.; Pertsch, T.; Lederer, F., Asymmetric transmission of linearly polarized light at optical metamaterials. *Phys. Rev. Lett.* **2010**, *104*, 253902.
- (11) Singh, R.; Plum, E.; Menzel, C.; Rockstuhl, C.; Azad, A. K.; Cheville, R. A.; Lederer, F.; Zhang, W.; Zheludev, N. I., Terahertz metamaterial with asymmetric transmission. *Phys. Rev. B* **2009**, *80*, 153104.
- (12) Schwanecke, A. S.; Fedotov, V. A.; Khardikov, V. V.; Prosvirnin, S. L.; Chen, Y.; Zheludev, N. I., Nanostructured metal film with asymmetric optical transmission. *Nano Lett.* **2008**, *8*, 2940-2943.
- (13) Drezet, A.; Genet, C.; Laluet, J. Y.; Ebbesen, T. W., Optical chirality without optical activity: How surface plasmons give a twist to light. *Opt. Express* **2008**, *16*, 12559-12570.
- (14) Plum, E.; Fedotov, V. A.; Zheludev, N. I., Asymmetric transmission: a generic property of two-dimensional periodic patterns. *J. Opt.* **2011**, *13*, 024006.
- (15) Menzel, C.; Rockstuhl, C.; Lederer, F., Advanced jones calculus for the classification of periodic metamaterials. *Phys. Rev. A* **2010**, *82*, 053811.
- (16) Niemi, T.; Karilainen, A. O.; Tretyakov, S. A., Synthesis of polarization transformers. *IEEE Trans. Antennas Propag.* **2013**, *61*, 3102-3111.



- (17) Kang, M.; Chen, J.; Cui, H. X.; Li, Y. N.; Wang, H. T., Asymmetric transmission for linearly polarized electromagnetic radiation. *Opt. Express* **2011**, *19*, 8347-8356.
- (18) Mutlu, M.; Akosman, A. E.; Serebryannikov, A. E.; Ozbay, E., Asymmetric transmission of linearly polarized waves and polarization angle dependent wave rotation using a chiral metamaterial. *Opt. Express* **2011**, *19*, 14290-14299.
- (19) Huang, C.; Feng, Y. J.; Zhao, J. M.; Wang, Z. B.; Jiang, T., Asymmetric electromagnetic wave transmission of linear polarization via polarization conversion through chiral metamaterial structures. *Phys. Rev. B* **2012**, *85*, 195131.
- (20) Malinauskas, M.; Farsari, M.; Piskarskas, A.; Juodkasis, S., Ultrafast laser nanostructuring of photopolymers: A decade of advances. *Physics Reports* **2013**, *533*, 1-31.
- (21) Farsari, M.; Chichkov, B. N., Two-photon fabrication. *Nature Photonics* **2009**, *3*, 450-452.
- (22) Vasilantonakis, N.; Terzaki, K.; Sakellari, I.; Purlys, V.; Gray, D.; Soukoulis, C. M.; Vamvakaki, M.; Kafesaki, M.; Farsari, M., Three-dimensional metallic photonic crystals with optical bandgaps. *Adv. Mater.* **2012**, *24*, 1101-1105.
- (23) Terzaki, K.; Vasilantonakis, N.; Gaidukeviciute, A.; Reinhardt, C.; Fotakis, C.; Vamvakaki, M.; Farsari, M., 3d conducting nanostructures fabricated using direct laser writing. *Opt. Mater. Express* **2011**, *1*, 586-597.
- (24) Zhou, J. F.; Chowdhury, D. R.; Zhao, R. K.; Azad, A. K.; Chen, H. T.; Soukoulis, C. M.; Taylor, A. J.; O'Hara, J. F., Terahertz chiral metamaterials with giant and dynamically tunable optical activity. *Phys. Rev. B* **2012**, *86*, 035448.
- (25) Wang, B. N.; Zhou, J. F.; Koschny, T.; Soukoulis, C. M., Nonplanar chiral metamaterials with negative index. *Appl. Phys. Lett.* **2009**, *94*, 151112.
- (26) Li, Z. F.; Mutlu, M.; Ozbay, E., Highly asymmetric transmission of linearly polarized waves realized with a multilayered structure including chiral metamaterials. *J. Phys. D-Appl. Phys.* **2014**, *47*, 075107.
- (27) Mazneva, A. A.; Every, A. G.; Wright O. B., Reciprocity in reflection and transmission: What is a 'phonon diode'? *Wave Motion* **2013**, *50*, 776-784.
- (28) Pendry, J.; Holden, A.; Stewart, W.; Youngs, I., Extremely low frequency plasmons in metallic mesostructures. *Phys. Rev. Lett.* **1996**, *76*, 4773.
- (29) Bassiri, S.; Papas, C. H.; Engheta, N., Electromagnetic wave propagation through a dielectric-chiral interface and through a chiral slab. *J. Opt. Soc. Am. A* **1988**, *5*, 1450-1459.
- (30) Zhou, J.; Koschny, Th.; Kafesaki, M.; Economou, E. N.; Pendry J. B.; Soukoulis, C. M., Saturation of the magnetic response of split-ring resonators at optical frequencies, *Phys. Rev. Lett.* **2005**, *95*, 223902.
- (31) Penciu, R. S.; Kafesaki, M.; Koschny, Th.; Economou, E. N.; Soukoulis, C. M., Magnetic response of nanoscale left-handed metamaterials, *Phys. Rev. B* **2010**, *81*, 235111.
- (32) Johnson, P. B.; Christy, R. W., Optical constants of the noble metals. *Phys. Rev. B* **1972**, *6*, 4370.